Modeling Light–Tissue Interaction in Optical Coherence Tomography Systems

3

Peter E. Andersen, Thomas M. Jørgensen, Lars Thrane, Andreas Tycho, and Harold T. Yura

Keywords

Absorption • Light propagation • Light tissue interaction • Optical coherence tomography • Scattering • Theoretical model

3.1 Introduction

Optical coherence tomography (OCT) has developed rapidly since its potential for applications in clinical medicine was first demonstrated in 1991 [1]. OCT performs high-resolution, cross-sectional tomographic imaging of the internal microstructure in materials and biologic systems by measuring backscattered or backreflected light.

Mathematical models [2–11] have been developed to promote understanding of the OCT imaging process and thereby enable the development of better imaging instrumentation and data processing algorithms. One of the most important issues in the modeling of OCT systems is the role of the multiple-scattered photons, an issue which has become fully understood through the works of Thrane et al. [12] and Turchin et al. [13] representing the most comprehensive modeling.

Experimental validation of models on realistic sample structures, e.g., layered sample structures, would require manufacturing of complex tissue phantoms with well-controlled optical properties. However, a useful alternative to validate the analytical predictions on such geometries is to apply a Monte Carlo (MC)-based simulation model [14], because there are few limitations on which geometries may be modeled using MC simulations. MC models for analyzing light propagation are based on

P.E. Andersen (✉) • T.M. Jørgensen • L. Thrane • A. Tycho
Department of Photonics Engineering, Technical University of Denmark, Roskilde, Denmark
e-mail: peta@fotonik.dtu.dk.

H.T. Yura
The Aerospace Corporation, Electronics and Photonics Laboratory, Los Angeles, CA, USA

W. Drexler, J.G. Fujimoto (eds.), *Optical Coherence Tomography*,
DOI 10.1007/978-3-319-06419-2_4

simulating the radiative equation of transfer by tracing a large number of energy packets each considered to represent a given component of the incident light energy [15, 16]. Hence, as a numerical experiment, one has full control of all parameters.

The scope of this chapter is to present analytical and numerical models that are able to describe the performance of OCT systems including multiple-scattering effects in heterogeneous media. Such models, where the contribution to the OCT signal from multiple-scattering effects is taken into account, are essential for the understanding and in turn optimization of OCT systems. An analytical model based on the extended Huygens–Fresnel (EHF) principle meeting these requirements is presented here. An MC analysis is presented in order to handle the modeling of heterodyne/coherent detection OCT systems with a radiative transfer-type photon packet MC approach. Using this MC model results are obtained, which validate the EHF model. In general, these models, analytical as well as numerical, may serve as important tools for improving the interpretation of OCT images.

3.1.1 Modeling Light–Tissue Interactions Relevant to OCT

Since the first paper describing the use of the OCT technique for noninvasive cross-sectional imaging in biological systems [1], various theoretical models of the OCT system have been developed. The primary motivation for deriving an appropriate model has been the potential optimization of the OCT technique leading to an improvement in imaging capabilities and to the possibility of extracting physical parameters.

The first theoretical models were based on single-scattering theory [2, 3]. These models are restricted to superficial layers of highly scattering tissue in which only single scattering occurs. Single scattering or single backscattering refers to photons which do not undergo scattering either to or from the backscattering plane of interest, i.e., ballistic photons.

At larger probing depths, however, the light is also subject to multiple scattering. The effects of multiple scattering have been investigated on an experimental basis [5], by using a hybrid Monte Carlo/analytical model [6] and analysis methods of linear systems theory [7], on the basis of solving the radiative transfer equation in the small-angle approximation [8, 13], by using models based on the extended Huygens–Fresnel (EHF) principle [9, 12, 17], and MC simulations [10, 14]. Note that modeling using MC simulations is treated in greater detail in Sect. 3.4.2.

In the present context, the main objective is the analysis of multiple-scattering effects. As shown by several investigations, the primary effects of multiple scattering are a reduction of the imaging contrast and resolution of the OCT system. In Ref. [4], the authors suggested solving the multiple-scattering problem by using the EHF principle [9] known from atmospheric propagation of laser beams [18]. Their analysis contains one important inaccuracy because in their end result, the ballistic component is included twice leading to erroneous calculations. As a result, their analysis should be applied with care. In addition, the effects of the so-called shower-curtain effect [18] are not accounted for in their analysis. Thrane et al. [12] succeeded in applying the EHF principle for the OCT geometry; see Sect. 4.2. Following their analysis,

Feng et al. [17] aimed at expanding on the use of EHF in modeling the OCT geometry. In particular, their aim is to simplify the analysis, but several mistakes are introduced in the attempt: firstly, an imaginary lens is introduced with the purpose of obviating the shower-curtain effect leading to errors in the final calculation of the OCT signal. Secondly, an erroneous lateral coherence length is introduced, i.e., the lateral coherence length should be calculated as resulting from reflecting off a rough surface and not, as done in Ref. [17], a specular surface. Hence, their model should be approached with caution.

A statistical optics approach to adequately model the effects of multiple scattering was proposed by Karamata et al. [19]. However, their analysis, based on a heuristic argument, is misleading and incorrect. The main error is due to their assumption regarding spatial coherence, where it is alleged that transverse spatial coherence is not degraded due to multiple scattering. The argument used by Karamata et al. [19] is valid only for the case of a focused beam reflecting off a rough surface with no scattering medium in between the reflection site and the collection aperture; see, for example, pages 210–211 of Ref. [20]. This is definitely not the case for OCT in turbid media (i.e., tissue). The degradation of spatial coherence of a beam propagating through a multiple-scattering media is well known and documented in the literature; see Ref. [21] and references therein. Therefore, the analysis given in Ref. [19] is not considered further, and the results and conclusions should not be used in modeling light propagation in turbid media.

Turchin et al. [13] expanded the analysis of Dolin [8] to an OCT geometry. Their analysis is based on the radiative transfer equation (RTE) in the small-angle approximation, of which Arnush [22] first obtained the closed-form solution. It should be noted that in this approximation, the solution of the RTE and the EHF is identical [23, 24]. In general, the analysis of Ref. [13] is consistent with that of the EHF model, which is presented below. However, technically there are two important differences that need to be pointed out. Firstly, the choice of scattering phase function in Ref. [13]: as in Ref. [12], the forward scattered part is modeled by a Gaussian distribution, but additionally a small backscattered fraction is included. This way of taking into account tissue backscattering was previously suggested by Raymer et al. [25–27] and discussed by Yura et al. [24]. However, it was not included in the EHF analysis of the OCT geometry [12], but it is incorporated below. Hence the RTE [13] and EHF [12] descriptions are equivalent. Secondly, Thrane et al. [12] present an analytical engineering expression for the OCT signal current based on an accurate analytical approximation for the irradiance distribution in the backscatter plane (see Appendix for details). Turchin et al. [13] do not use this approximation, and consequently their end results require numerical computations, which yield highly accurate values for the OCT signal current. They also obtain accurate results in the extraction of optical scattering properties of the sample, which is further addressed in Sect. 3.5.1. Furthermore, it is noted that the analysis of Turchin et al. [13] is restricted to the special case where the focusing lens in the sample arm is in direct contact with the tissue being investigated. This is in contrast to the analysis of Ref. [12] where the ABCD ray-matrix formalism was used to readily include an arbitrary configuration of the sample arm. Finally, in

contrast to the totally numerical results of Ref. [13], the multiple-scattering EHF analysis presented below yields accurate analytical expressions for the OCT signal for a wide range of optical configurations that both are amenable to physical interpretation (see, e.g., [28]) and are desirable for use in parametric studies for OCT system optimization.

Strictly speaking, the OCT model developed in Ref. [12] and further extended here is based on the assumption that the detected signal return arises only from photons that have been backscattered from a target layer selected by the coherence gate of the light source. Backscattered photons from the bulk tissue between the light source and the target layer have been assumed to be negligible in comparison with photons arising from the tissue discontinuity. Realistically, photons backscattered from the intervening bulk tissue whose optical path-length difference between the reference light is within the coherence length will also be detected. Bulk backscattered detected light contributes to the noise in the OCT signal because it does not furnish any local information about the target layer. Yao and Wang [29] used a Monte Carlo-based technique to simulate the OCT signal from homogeneous turbid medium. They considered a single mode fiber emitting a pencil beam that is in direct contact with the turbid medium and divided the OCT signal return into two categories: one from a target imaging layer in the medium (Class I photons) and the other from the intervening bulk tissue (Class II photons). The simulation results of Ref. [29] reveal that these two classes of photons have very different spatial and angular distributions which make OCT possible. The Class II signal has a much broader spatial distribution than the Class I signal. Although the spatial distributions of both signals broaden with probing depth, the Class II signal is broadened much faster than the Class I signal, and thus, limiting the detection area will reject most of the Class II signal. Additionally, Class II photons have a wider angular distribution than the corresponding Class I photons, and a correspondingly larger fraction of Class II photons that impinge on the detector area will not be effectively heterodyne coupled with the reference light. For large probing depths, however, the simulation results for the homogeneous turbid medium indicated that Class II signal photons will eventually become dominant. The actual crossover point is ultimately related to the efficiency of Class II signal rejection, whether or not the medium contains refractive index discontinuities, and the effects of Class II photon rejection due to imaging configurations such as dynamic focusing. With these considerations in mind, the extended Huygens–Fresnel-based OCT model developed in Ref. [12], updated to incorporate the attenuating effects of tissue backscatter, is presented below.

3.1.2 Organization of this Chapter

The chapter is divided into three sections covering specific topics in modeling OCT systems. In Sect. 3.2, an analytical model for the detected OCT signal is derived based on the EHF principle. In Sect. 3.3, the effects of multiple scattering on the detected Doppler OCT signal are investigated. In the field of biomedical optics, Monte Carlo simulations have already proved their value. In Sect. 3.4, an advanced

Monte Carlo model for calculating the OCT signal is presented, and comparisons to the analytical model are made. In general, good agreement is obtained, thus validating the EHF model. Section 3.5 overviews the impact of extracting optical scattering properties from OCT images on the diagnostic potential of OCT.

3.2 Analytical OCT Model Based on the Extended Huygens–Fresnel Principle

In the present section, a general theoretical description [12, 30, 31] of the OCT technique when used for imaging in highly scattering tissue is presented, which is valid for an arbitrary ABCD optical configuration. The description is based on the EHF principle. In a standard OCT system [1] with diffuse backscattering from the tissue discontinuity being probed, and a distance between the focusing lens and the tissue, the so-called shower-curtain effect [18, 32] is present, which is uniquely included in Ref. [12]. This effect is not described by previous ad hoc theoretical models [9]. Furthermore, because the sample arm focusing lens in Turchin et al. [13] is assumed to be in direct contact with the tissue being probed, shower-curtain effects are not present in the geometry and hence not in their analysis.

3.2.1 The Extended Huygens–Fresnel Principle

When an optical wave propagates through a so-called random medium, e.g., tissue, both the amplitude and phase of the electric field experience fluctuations caused by small random changes in the index of refraction across the sample. For tissue [33] it can in general be assumed that the depolarization term of the associated vectorial wave equation can be neglected, if the wavelength of the radiation, λ, is much smaller than l_0, where l_0 is a measure of the smallest random inhomogeneities in the medium [34, 35] (the structures that dominate light propagation in tissue, e.g., cells, have a size of 2 μm or more). With this assumption, the wave equation can be simplified to three scalar equations, one for each component of the field. Letting $U(\mathbf{R})$ denote one of the scalar components transverse to the direction of propagation along the positive z-axis, the following scalar stochastic equation is obtained:

$$\nabla^2 U + k^2 n^2(\mathbf{R}) U = 0, \tag{3.1}$$

where k is the wave number, $\mathbf{R}$ is a point in space, and $n(\mathbf{R})$ is the index of refraction. Considering a random medium, $n(\mathbf{R})$ acts as a stochastic variable for different realizations of tissue with given macroscopic optical parameters. Equation 3.1 cannot be solved exactly in closed form. Some early attempts to solve Eq. 3.1 were based on the geometric optics approximation [36], which ignores diffraction effects, and on perturbation theories widely known as the Born

approximation and Rytov approximation [37]. An alternative method was developed, independent of each other, by Lutomirski and Yura [38] and by Feizulin and Kravtsov [39]. This technique is called the extended Huygens–Fresnel (EHF) principle. It extends the Huygens–Fresnel principle to deal with media that exhibit a random spatial variation in the index of refraction. This principle follows directly from Green's theorem [40] and the Kirchhoff approximation [40] applied to the scalar wave equation together with the use of a field reciprocity theorem. Yura and Hanson [41, 42] have applied the EHF principle to paraxial wave propagation through an arbitrary ABCD system in the presence of random inhomogeneities. An arbitrary ABCD system refers to an optical system that can be described by the so-called ABCD ray-transfer matrix [43]. For the present cases of interest, the ABCD ray-transfer matrix is real, and the field in the output plane is then given by [41]

$$U(\mathbf{r}) = \int U_0(\mathbf{p}) G(\mathbf{p},\mathbf{r}) d\mathbf{p} \tag{3.2}$$

where $\mathbf{r}$ and $\mathbf{p}$ are two-dimensional vectors transverse to the optical axis in the output plane and input plane, respectively. The spatial integrals are to be carried out over the entire plane in question. The quantity $U_0(\mathbf{p})$ is the field in the input plane, and $G(\mathbf{p},\mathbf{r})$ is the EHF Green's function describing the response at $\mathbf{r}$ due to a point source at $\mathbf{p}$ given by [38, 41]

$$G(\mathbf{p},\mathbf{r}) = G_0(\mathbf{p},\mathbf{r}) \exp[i\varphi(\mathbf{p},\mathbf{r})], \tag{3.3}$$

where $G_0(\mathbf{p},\mathbf{r})$ is Huygens–Fresnel Green's function for propagation through an ABCD system in the absence of random inhomogeneities and $\varphi(\mathbf{p},\mathbf{r})$ is the random phase of a spherical wave propagating in the random medium from the input plane to the output plane. Huygens–Fresnel Green's function $G_0(\mathbf{p},\mathbf{r})$ is given by [41]

$$G_0(\mathbf{p},\mathbf{r}) = -\frac{ik}{2\pi B} \exp\left[-\frac{ik}{2B}\left(Ap^2 - 2\mathbf{p}\cdot\mathbf{r} + Dr^2\right)\right], \tag{3.4}$$

where A, B, and D are the ray-matrix elements for propagation from the input plane to the output plane.

3.2.2 Calculating the OCT Signal: Time Domain

A time-domain OCT system [1] is based on a broad bandwidth light source (SLD), a Michelson interferometer with a movable reference mirror, and a photodetector. The rotationally symmetric sample arm geometry of such an OCT system is depicted in Fig. 3.1, where a lens with focal length f is placed at a distance d from the tissue surface. The optical path length of the reference arm in the

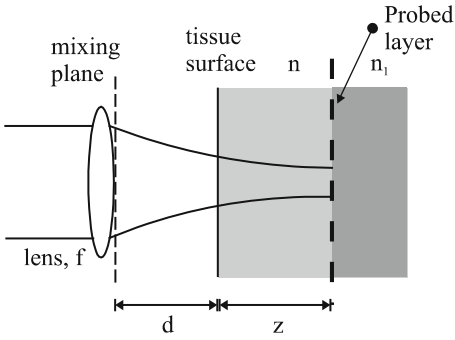

Fig. 3.1 Sample arm geometry of the OCT system

Michelson interferometer is matched to the optical depth of the focal plane, whereby the configuration – due to backscattering – is probing the layer of the tissue coinciding with the focal region.

For the wavelengths of interest in the NIR region and, e.g., in the case of human skin, light scattering in the bulk tissue is predominantly taking place in the forward direction [44]. Hence, the scattering phase function $\sigma(\theta,z)$ can be modeled as a sum of a small-angle scattering phase function $\sigma_1(\theta,z)$ that tends to zero for $\theta > \pi/2$ and a constant but relative small isotropic term included to incorporate a backscattered contribution [8, 13]:

$$\sigma(\theta, z) = [1 - 2p_b(z)]\sigma_1(\theta, z) + 2p_b(z), \tag{3.5}$$

where $p_b(z)$ denotes the backscattering coefficient as a function of the depth. For tissues, the quantity p_b will normally be much smaller than unity, i.e., $p_b << 1$; see, for example, Ref. [13].

It was noted above that the EHF principle is based on the paraxial approximation and therefore valid for small-angle forward scattering. In particular, it can be shown that the paraxial approximation is valid up to 30°, i.e., 0.5 rad [43]. Because most tissues are characterized by *rms* scattering angles below this limit, the EHF principle may be used to describe light propagation in tissue retaining both amplitude and phase information. Also, the bulk tissue absorption is neglected in the present calculation, because in the case of most tissues, the scattering essentially accounts for the signal attenuation [44]. Basically including the absorption would result in an overall exponential decay. Thus, bulk homogeneous tissue is characterized by a scattering coefficient μ_s, a root-mean-square scattering angle θ_{rms} or asymmetry parameter g [45], and a mean index of refraction n. Furthermore, the bulk tissue is modeled as a material with scatterers randomly distributed over the volume of interest.

Consider an optical field that is narrowband and non-monochromatic, i.e., the spectral width of the light source $\Delta\nu$ is much smaller than the center frequency ν. Light sources characterized as "broad band" in relation to OCT also fulfills this condition. At a spatial coordinate $\mathbf{p}$ and time t, such an optical field may be expressed in terms of a (temporally) slowly varying complex amplitude $A(t)$

where the characteristic temporal scale of the complex envelope amplitude A is much less than $1/\nu_0$. In addition it is assumed that the reference field, U_R, and the incident sample field, U_{Si}, are of Gaussian shapes:

$$U_R(\mathbf{p},t) = \sqrt{\frac{P_R}{\pi w_0^2}\exp\left[-\frac{|\mathbf{p}|^2}{2}\left(\frac{1}{w_0^2}+\frac{ik}{f}\right)\right]}A(t)\exp[i\omega_R t+\varphi_R(t)], \tag{3.6}$$

$$U_{Si}(\mathbf{p},t) = \sqrt{\frac{P_s}{\pi w_0^2}\exp\left[-\frac{|\mathbf{p}|^2}{2}\left(\frac{1}{w_0^2}+\frac{ik}{f}\right)\right]}A(t)\exp[i\omega_s t+\varphi_s(t)], \tag{3.7}$$

where P_R and P_S are the powers of the reference and input sample beams, respectively; w_0 is the $1/e$ intensity radius of these beams in the lens plane, $k = 2\pi/\lambda$; λ is the center wavelength of the source in vacuum; ω_R and ω_S are the angular frequencies of the reference and input sample beams, respectively; and φ_R and φ_S are the phases of the reference field and input sample field, respectively.

The mixing of the backscattered or reflected sample field U_S from the probed layer with the reference field U_R on the photodetector of the OCT system gives rise to a heterodyne signal current $i(z)$ [9]:

$$i(z) \propto |\gamma(\tau)|\mathrm{Re}\left[\int U_R(\mathbf{p})\,U_S^*(\mathbf{p})d\mathbf{p}\right], \tag{3.8}$$

where the integration is taken over the area of the photodetector. Re[·] denotes the real part, and τ denotes the time difference between the propagation times of the reference and sample beams. $|\gamma(\tau)|$ is the modulus of the normalized temporal coherence function of the source.

Because a random medium is considered, the mean square heterodyne signal current $\langle i^2(z)\rangle$ should be calculated, which is proportional to the heterodyne signal power. It can be shown to be given by [9, 18]:

$$\langle i^2(z)\rangle = 2\alpha^2|\gamma(\tau)|^2\mathrm{Re}\left[\iint \Gamma_S(\mathbf{p}_1,\mathbf{p}_2;z)\Gamma_R(\mathbf{p}_1,\mathbf{p}_2)d\mathbf{p}_1 d\mathbf{p}_2\right], \tag{3.9}$$

where

$$\Gamma_R(\mathbf{p}_1,\mathbf{p}_2) = \langle U_R(\mathbf{p}_1)U_R^*(\mathbf{p}_2)\rangle = U_R(\mathbf{p}_1)U_R^*(\mathbf{p}_2) \tag{3.10}$$

$$\Gamma_s(\mathbf{p}_1,\mathbf{p}_2;z) = \langle U_s(\mathbf{p}_1;z)U_s^*(\mathbf{p}_2;z)\rangle \tag{3.11}$$

are the mutual coherence functions of the reference and the reflected sample optical fields in the mixing plane. The angular brackets denote an ensemble

average over the statistical properties of the tissue. Physically, the heterodyne mixing process takes place on the photosensitive surface of the detector in the focal plane of the "mixing" lens. However, Fried [46] has shown mathematically that one can identically compute the mean square heterodyne photocurrent in a plane directly in front of the mixing lens at the side facing the sample, and, accordingly, $\mathbf{p}_1$, $\mathbf{p}_2$ are two-dimensional vectors in this plane transverse to the optical axis. The quantity α is a conversion factor for power to current and equals $(q_e\eta/h\nu)$, where q_e is the electronic charge, η the detector quantum efficiency, ν the optical center frequency, and h Planck's constant. In the present analysis, without loss of generality, the temporal coherence function is approximated with a rectangular function of width τ_c, the coherence time of the source.

Details of the derivation of the mutual coherence function Γ_S are given in Appendix under the assumption that the forward propagated light can be considered statistically independent from the backscattered light. To obtain a closed-form expression including the intermediate ranges of propagation, the single-scattering solution and the solution for large optical depths are interpolated, as outlined in Appendix, yielding the following squared signal contribution from within the coherence gate around the depth z:

$$\left\langle i^2(z)\right\rangle_{coh\_gate} \approx \frac{2\alpha^2 P_R P_S \sigma_b}{\pi^2} \int \left[\frac{e^{-\mu_s z}\exp\left\{-r^2/w_H^2\right\}}{w_H^2} + \frac{(1-e^{-\mu_s z})e^{-2p_b\mu_s z}\exp\left\{-r^2/w_S^2\right\}}{w_S^2}\right]^2 d\mathbf{r}, \tag{3.12}$$

where the effective backscattering cross section of the layer being probed is defined as $\sigma_b = 4\pi p_b \mu_s l_c/k^2$. Here l_c denotes the coherence length of the source given by $c\tau_c$. In Eq. 3.12 it is assumed that $\mu_s l_c << 1$.

The quantities w_H and w_S are the $1/e$ irradiance radii in the target plane in the absence and presence of scattering, respectively, given by [12]

$$w_H^2 = w_0^2\left(A - \frac{B}{f}\right)^2 + \left(\frac{B}{kw_0}\right)^2, \tag{3.13}$$

$$w_S^2 = w_0^2\left(A - \frac{B}{f}\right)^2 + \left(\frac{B}{kw_0}\right)^2 + \left(\frac{2B}{k\rho_0}\right)^2, \tag{3.14}$$

where ρ_0 denotes the lateral coherence length of the reflected sample field in the plane in which the mixing calculated [12]

$$\rho_0(z) = \sqrt{\frac{3}{\mu_s z}}\frac{\lambda}{\pi\theta_{\text{rms}}}\left(\frac{nB}{z(1-2p_b)}\right). \tag{3.15}$$

Here the root-mean scattering angle, θ_{rms}, is related to the anisotropy parameter g:

$$\theta_{\mathrm{rms}} \approx \sqrt{2(1-g)}. \tag{3.16}$$

Performing the integration over the probed layer (see Fig. 3.1) in Eq. 3.12 and simplifying, the following expression for the mean square heterodyne signal current is obtained:

$$\begin{aligned}\left\langle i^2(z)\right\rangle_{coh\_gate} &\approx \frac{\alpha^2 P_R P_s \sigma_b}{\pi w_H^2} \\ &\times \left[e^{-2\mu_s z} + \frac{4e^{-\mu_s z}e^{-2p_b\mu_s z}(1-e^{-\mu_s z})}{1+\frac{w_S^2}{w_H^2}} + (1-e^{-\mu_s z})^2 e^{-4p_b\mu_s z}\frac{w_H^2}{w_S^2} \right] \\ &= \left\langle i^2\right\rangle_0 \Psi(z).\end{aligned} \tag{3.17}$$

Assuming $p_b << 1$, Eq. 3.17 reduces to

$$\begin{aligned}\left\langle i^2(z)\right\rangle_{coh\_gate} &\approx \frac{\alpha^2 P_R P_s \sigma_b}{\pi w_H^2} \\ &\times \left[e^{-2\mu_s z} + \frac{4e^{-\mu_s z}(1-e^{-\mu_s z})}{1+\frac{w_S^2}{w_H^2}} + (1-e^{-\mu_s z})^2 \frac{w_H^2}{w_S^2} \right] \\ &= \left\langle i^2\right\rangle_0 \Psi(z).\end{aligned} \tag{3.18}$$

The quantity $\langle i^2\rangle_0 = \alpha^2 P_R P_S \sigma_b/\pi(w_H)^2$ is the mean square heterodyne signal current in the absence of scattering, and the terms contained in the brackets are the heterodyne efficiency factor $\Psi(z)$. The quantity $\Psi(z)$ is the reduction in the heterodyne signal-to-noise ratio due to the scattering of the tissue. The first term in the brackets of Eq. 3.17 represents the contribution due to single scattering. The third term is the multiple-scattering term, and the second term is the cross term. Physically, the cross term is the coherent mixing of the unscattered and the multiple-scattered light. A comparison between the analytical approximation of $\Psi(z)$, given in Eq. 3.17, and the exact numerical calculation is given in Ref. [47] showing reasonable agreement. The validity of the above expression has been explored by comparing the model with advanced Monte Carlo studies and confirms that the analytical result provides a feasible model for investigating the qualitative behavior of the OCT configuration; see Sect. 3.4.

3.2.2.1 Dynamic Focusing: Diffuse Reflectance

If one applies dynamic focusing, the focal plane will ideally be arranged to move in accordance with the position of the coherence gate. This situation can be analyzed by setting $fA = B$ and $A = 1$ in Eqs. 3.13 and 3.14:

$$w_H = \frac{f}{kw_0}, w_S = \sqrt{w_H^2 + \left(\frac{2f}{k\rho_0}\right)^2}, \tag{3.19}$$

$$\frac{w_H^2}{w_S^2} = \frac{1}{1 + \left(\frac{2w_0}{\rho_0(z)}\right)^2}. \tag{3.20}$$

For lateral separations much less (greater) than the coherence length, $\rho_0(z)$, the field can be considered to be mutually coherent (incoherent). Because of the diffuse backscattering from the layer being probed, $\rho_0(z)$ is determined only by the propagation back through the tissue from this layer to the mixing plane. As a consequence, $\rho_0(z)$ is the lateral coherence length in the mixing plane of a point source located in the tissue plane being probed. For the geometry of interest, it can be shown [47] that

$$\rho_0(z) = \sqrt{\frac{3}{\mu_s z}} \frac{\lambda}{\pi\theta_{\text{rms}}} \left(\frac{z + nd(z)}{z\sqrt{1 - 2p_b}}\right) \tag{3.21}$$

where $d(z) = f - z/n$, and $\theta_{\text{rms}} \approx [2(1 - g)]^{1/2}$. The second term in the brackets of Eq. 3.21 indicates that the lateral coherence length increases with increasing distance between the tissue surface and the mixing plane.

The dependence of the lateral coherence length on the position of the scattering medium relative to the observation plane is the so-called shower-curtain effect [18, 32]. In general, the shower-curtain effect implies that the lateral coherence length obtained for the case when the scattering medium is close to the radiation source is larger than for the case when the scattering medium is close to the observation plane. Physically, this is due to the fact that a distorted spherical wave approaches a plane wave as it further propagates through a non-scattering medium. As a consequence, e.g., from a distance, one can see a person immediately behind a shower curtain, but the person cannot see you. The effect is well known for light propagation through the atmosphere as discussed by Dror et al. [32], but has been omitted in previous theoretical OCT models [9]. However, due to the finite distance between the focusing lens and the tissue, the effect is inevitably present in practical OCT systems. Finally, the reflection characteristics of the tissue play a vital role for the shower-curtain effect.

It is only in the very superficial layers of highly scattering tissue that it is possible to achieve diffraction-limited focusing. In this region, the spot size is given by $2w_H$. At deeper probing depths, the spot size is dependent on the scattering properties and

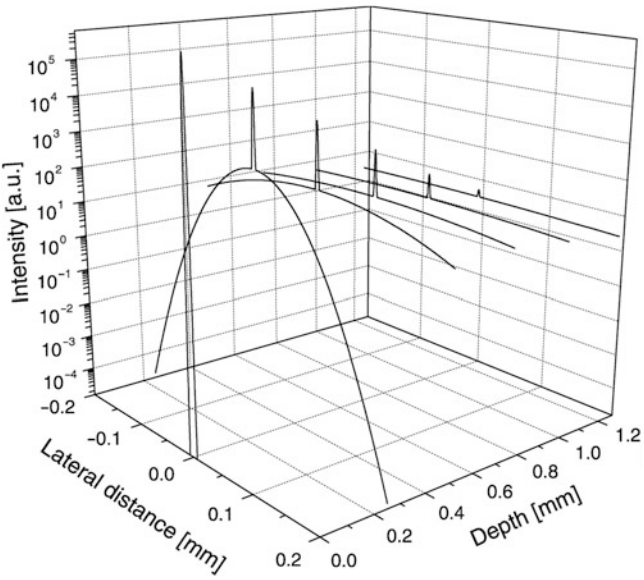

Fig. 3.2 The intensity pattern as a function of the probing depth z in the tissue ($\lambda = 814$ nm, $\mu_s = 10\ \text{mm}^{-1}$, $g = 0.955$ ($\theta_{\text{rms}} = 0.3$ rad), $n = 1.4, f = 5$ mm, $w_0 = 0.5$ mm)

given by $2w_S$. It is seen from Eqs. 3.20 and 3.21 that the spot size is degraded due to multiple scattering when the probing depth is increased. This is illustrated in Fig. 3.2, where the intensity pattern is shown as a function of the probing depth z in the tissue using Eq. 3.72, thus illustrating spot size degradation in, e.g., microscopy.

From Eq. 3.18 an expression for the OCT signal for large optical depths can be obtained as

$$\left\langle i^2(z)\right\rangle \propto \frac{\exp(-4p_b\mu_s z)}{\mu_s(1-g)z^3}, \mu_s z >> 1. \tag{3.22}$$

From this expression it is observed that the denominator is proportional to the reduced scattering coefficient $\mu_s(1\text{-}g)$, while the numerator will be close to 1 for small values of p_b. Consequently, if the signal for large optical depths is observed, it cannot be expected to derive both μ_s and g from the measured depth profiles.

3.2.2.2 Dynamic Focusing: Specular Reflectance

If, instead of diffuse backscattering, one had a specular reflection at the layer being probed, the corresponding mutual coherence function for plane waves would apply. Using this mutual coherence function and $p_b << 1$, the following expression is obtained for the heterodyne efficiency factor:

$$\Psi(z) = \left[e^{-2\mu_s z} + \left(1 - e^{-2\mu_s z}\right) \frac{w_H^2}{w_s^2} \right] \tag{3.23}$$

and

$$\rho_0(z) = \sqrt{\frac{1}{2\mu_s z}} \frac{\lambda}{\pi \theta_{rms}}. \tag{3.24}$$

It is obvious from Eq. 3.24 that the shower-curtain effect would not be present in the case of specular reflection at the tissue discontinuity, in contrast to the case of diffuse backscattering. However, it is important to note that it is diffuse backscattering which actually occurs in the case of tissue.

3.2.2.3 Collimated Sample Beam

In the case of a collimated sample beam, the expressions for w_H and w_S in Eqs. 3.13 and 3.14 need to be rewritten:

$$w_H^2 = \lim_{f \to \infty} \left[w_0^2 \left(1 - \frac{d + z/n}{f} \right)^2 + \left(\frac{d + z/n}{k w_0} \right)^2 \right] = w_0^2 + \left(\frac{d + z/n}{k w_0} \right)^2 \tag{3.25}$$

$$\begin{aligned} w_S^2 &= \lim_{f \to \infty} \left[w_H^2 + \left(\frac{2(d + z/n)}{k \rho_0} \right)^2 \right] \\ &= w_0^2 + \left(\frac{d + z/n}{k w_0} \right)^2 + \left(\frac{2(d + z/n)}{k \rho_0} \right)^2, \end{aligned} \tag{3.26}$$

where it has been used that $A = 1$ and $B = d + z/n$. In order to find the heterodyne efficiency factor, these expressions must be inserted in Eq. 3.17, and moreover, the expression for ρ_0 should be chosen in accordance with the reflection characteristics of the probed layer.

3.2.2.4 Numerical Results

In Fig. 3.3, the calculated heterodyne efficiency factor $\Psi(z)$ from Eq. 3.18 is shown as a function of depth z of the tissue sample for typical parameters of human skin tissue. The curves are shown for the cases of diffuse backscattering with (dashed) and without (dash-dot) the shower-curtain effect included and for the specular reflection (solid), respectively. In addition, the case of pure single scattering (dotted) is included for comparison. At shallow depths single backscattering dominates. Due to multiple scattering, the slope is changed and $\Psi(z)$ becomes almost constant for three cases (curves 1–3). The important difference is, however, that the change of slope occurs at different depths. This is due to the shower-curtain effect leading to an appreciable

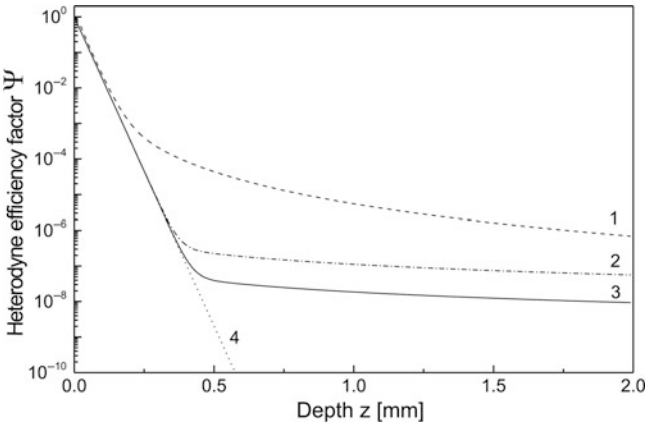

Fig. 3.3 $\Psi(z)$ as a function of z for diffuse backscattering with the shower-curtain effect included (curve 1) and for specular reflection (curve 3). Curve 2 is calculated for diffuse backscattering without the shower-curtain effect, and curve 4 is the case of pure single backscattering; $\lambda = 814$ nm, $\mu_s = 20\ \text{mm}^{-1}$, $g = 0.955$ ($\theta_{\text{rms}} = 0.3$ rad), $n = 1.4$, $f = 5$ mm, $w_0 = 0.5$ mm (From Ref. [12])

enhancement of $\Psi(z)$ and with it the heterodyne signal, which is obtained by comparing curves 1 and 2 in Fig. 3.3. Physically, this increase in the heterodyne signal is due to an enhanced spatial coherence of the multiple-scattered light.

In Fig. 3.4, $\Psi(z)$ from Eq. 3.18 is shown as a function of depth z for $\mu_s = 10\ \text{mm}^{-1}$ and three values of g within the range of validity of the EHF principle. The curves are computed for the case of diffuse backscattering. This figure demonstrates the degree of sensitivity of the heterodyne efficiency factor with respect to changes in the asymmetry parameter. Moreover, in Fig. 3.5, $\Psi(z)$ from Eq. 3.18 is shown as a function of depth z for $g = 0.95$ and three values of μ_s within the range of interest with respect to tissue [44]. The curves are again computed for the case of diffuse backscattering. This figure demonstrates the degree of sensitivity of the heterodyne efficiency factor with respect to changes in the scattering coefficient.

3.2.2.5 Choice of Scattering Function

In the present modeling of the OCT geometry, a Gaussian volume scattering function [20] for the forward scattered part is used; see Eqs. 3.5 and 3.64. The motivation for this choice of scattering function is the ability to obtain an accurate analytical engineering approximation, valid for all values of the optical depth. Using the Henyey–Greenstein scattering function [48], which is widely used in approximating the angular scattering dependence of single-scattering events in some biological media [44, 49], the corresponding analytical approximation is not as accurate as for the case of a Gaussian scattering function. However, a numerical computation using the exact expressions may be carried out instead. Hence, both scattering functions may be used in the modeling of the OCT geometry presented in this chapter.

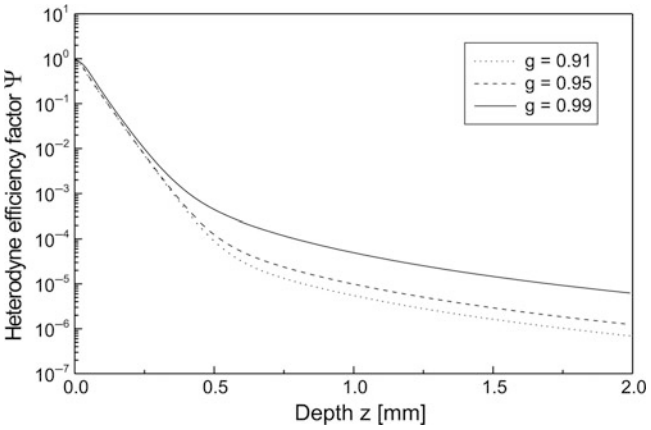

Fig. 3.4 $\Psi(z)$ as a function of z for $\mu_s = 10\ \text{mm}^{-1}$ and three values of g. The curves are for the case of a diffuse backscattering at the discontinuity and inclusion of the shower-curtain effect ($\lambda = 814$ nm, $n = 1.4, f = 5$ mm, $w_0 = 0.5$ mm)

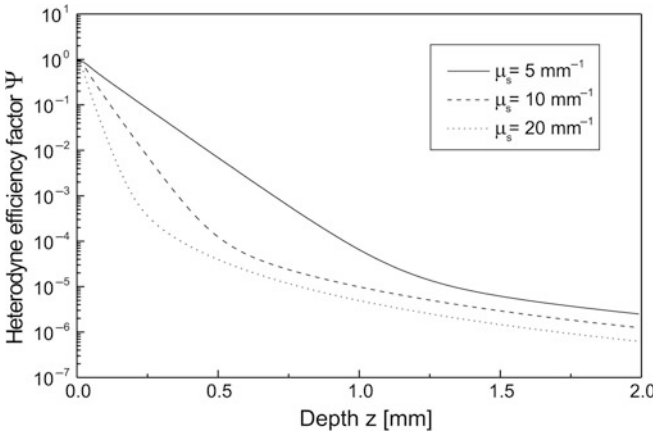

Fig. 3.5 $\Psi(z)$ as a function of z for $g = 0.95$ and three values of μ_s within a range of interest with respect to tissue. The curves are for the case of a diffuse backscattering at the discontinuity and inclusion of the shower-curtain effect ($\lambda = 814$ nm, $n = 1.4, f = 5$ mm, $w_0 = 0.5$ mm)

3.2.2.6 Signal-to-Noise Ratio (SNR) and Estimation of the Maximum Probing Depth

Without loss of generality, an OCT system with shot-noise-limited operation is considered here for calculating the signal-to-noise ratio (SNR) with the purpose of estimating the maximum probing depth. The only significant source of noise is the shot noise caused by the reference beam. For a photoconductive detector, the mean square noise power N_p can then be expressed as [50]

$$N_p = 2\alpha q_e G_{ca}^2 R_l B_w P_R, \tag{3.27}$$

where R_l is the resistance of the load, G_{ca} the gain associated with the current amplifier, and B_w the system bandwidth. The corresponding mean heterodyne signal power $S(z)$ is given by [46]

$$S(z)\langle i^2(z)\rangle G_{ca}^2 R_l \tag{3.28}$$

where $\langle i^2(z)\rangle$ is given by Eq. 3.17. Hence, the mean signal-to-noise ratio $SNR(z)$ is given by

$$SNR(z) = \frac{S(z)}{N_p} = (SNR)_0 \Psi(z), \tag{3.29}$$

where the signal-to-noise ratio in the absence of scattering $(SNR)_0$ is given by

$$(SNR)_0 = \frac{\eta P_S}{2h\nu B_w}\left(\frac{\sigma_b}{\pi w_H^2}\right). \tag{3.30}$$

In the case of interest where the focal plane coincides with the probed layer, the following expression for $(SNR)_0$ is obtained:

$$(SNR)_0 = \frac{4p_b \eta P_S}{h\nu B_w}\left(\frac{w_0}{f}\right)^2, \tag{3.31}$$

where it has been used that $\sigma_b = 4\pi p_b \mu_s l_c / k^2$.

The maximum probing depth is of considerable interest in the characterization and optimization of an OCT system when used for imaging in highly scattering tissue. The maximum probing depth may be calculated by using the model presented above. Details of the calculation are found in Ref. [31], where the calculation of the maximum probing depth z_{max} is based on the minimum acceptable SNR in the case of shot-noise-limited detection. In the calculations, a value of 3 is used as the minimum acceptable signal-to-noise ratio, i.e., $SNR(z_{max}) = 3$.

An important conclusion of Ref. [31] is that, in general, z_{max} depends on the focal length at small values of the scattering coefficient, but is independent of the focal length at larger values of the scattering coefficient. A similar behavior is observed for z_{max} as a function of μ_s and the $1/e$ intensity radius of the sample beam being focused. This behavior is due to multiple scattering of the light in the tissue. At scattering coefficients found in human skin tissue [44, 51], for example, it is concluded that the maximum probing depth is independent of the focal length f. This is an important conclusion because the depth of focus and the lateral resolution of the OCT system may then be chosen independently of z_{max}. For example, if no scanning of the focal plane in the tissue is desirable and, therefore, a large depth of

focus has been chosen, the same maximum probing depth is obtained as for a system with a short depth of focus where the focal plane is scanned to keep it matched to the reference arm. This conclusion is not surprising or contrary to assumptions already held in the field. However, the theoretical analysis in this section provides a theoretical foundation for such statements. Moreover, this agreement may also be taken as a further validation of the OCT model presented here.

3.3 Doppler OCT Analysis

Noninvasive localization and measurement of blood flow is of great interest in many medical applications, e.g., ophthalmology, dermatology, and gastroenterology. Optical Doppler tomography (ODT) [52, 53] combines Doppler velocimetry and optical coherence tomography. Thus, ODT is feasible for noninvasive localized diagnostics of particle flow velocity in highly scattering media, and it is important for functional imaging. In contrast to conventional OCT, where the reflectivity profile of the sample is obtained by envelope detection of the interferometric signal, ODT employs coherent phase-sensitive demodulation of the heterodyne detector current to obtain depth profiles of blood flow velocity. Basically, depth-resolved velocity estimates are obtained directly from the corresponding mean [52, 53] or standard deviation [54, 55] of the observed Doppler-frequency spectrum.

In this section, the results of a theoretical analysis of ODT based on EHF with multiple-scattering effects included are presented. Experiments by Yazdanfar et al. [56] suggest the presence of multiple-scattering effects in ODT. Another study also confirmed the impact of multiple-scattering effects estimating the impact on the determination of flow parameters [57]. The purpose of the analysis below is to determine how multiple scattering affects the estimation of the depth-resolved localized flow velocity, i.e., to obtain the dependence of the mean and standard deviation of the Doppler-frequency spectrum on the scattering properties of the medium.

3.3.1 Multiple-Scattering Effects in ODT

The ODT probe geometry being analyzed is shown in Fig. 3.6. In the absence of multiple scattering, and if the scattering geometry is precisely known, an estimate of the blood flow velocity at a given probing depth can be obtained as [52, 53]

$$V = \frac{f_S \lambda_0}{2n \cos \varepsilon}, \tag{3.32}$$

where λ_0 is the center wavelength of the light source, n is the index of refraction of blood, ε is the angle between the incident light and the direction of blood flow, and f_S is the centroid frequency of each depth-resolved spectrum, which is used as a measure of the corresponding backscattered Doppler frequency.

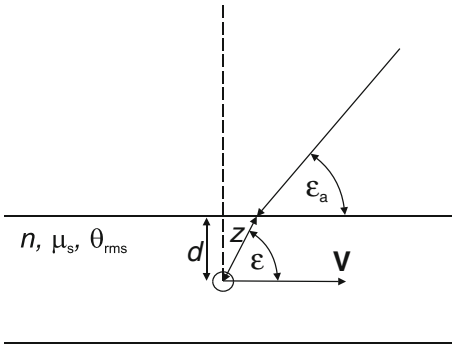

Fig. 3.6 The ODT probe geometry

In a multiple-scattering analysis of ODT, two effects must be taken into account: (a) the incident light on a moving particle contains a stochastic distribution of wave vectors at each optical frequency, and (b) in the round-trip propagation path to the backscattering event, the light will accumulate a random series of Doppler shifts due to the light being scattered by moving constituents along the path. Taking these multiple-scattering effects into account, the following equation for the mean Doppler shift may be derived [58]:

$$\overline{f}_D(d) = \frac{2n\cos\varepsilon}{\lambda_0}\left\{V(d)\exp\left(-\left\langle\theta^2\right\rangle/2\right) + \overline{V}(d)\left[1-\exp\left(-\left\langle\theta^2\right\rangle/2\right)\right]\right\}, \tag{3.33}$$

where $\langle\theta^2\rangle = \mu_s z\theta^2{}_{\mathrm{rms}}$. The quantities μ_s and θ_{rms} are the scattering coefficient and root-mean-square scattering angle of blood, respectively, and the probing depth $z = d/\sin\varepsilon$, where d is the transversal position in the vessel as indicated in Fig. 3.6. Furthermore, $V(d)$ is the flow velocity as a function of the transversal position in the vessel, and $\overline{V}$ is the mean velocity of the flow along the propagation path to the probing depth z. If multiple-scattering effects are neglected, Eq. 3.33 reduces to Eq. 3.32 as expected. In addition, for a constant velocity profile where $\overline{V} = V_0$, Eq. 3.33 yields $\overline{f}_D = 2V_0 n\cos\varepsilon/\lambda_0$ in agreement with Eq. 3.32, i.e., no multiple-scattering effects are present in this case as expected [59]. In the case of laminar flow in the vessel, the velocity and mean velocity profiles are given by [58]

$$V(d) = V_0\left[1-(1-d/a)^2\right] \quad \text{for} \quad 0 \le d \le 2a \tag{3.34}$$

$$\overline{V}(d) = V_0\frac{d}{a}\left(1-\frac{d}{3a}\right), \tag{3.35}$$

where a and V_0 are the radius of the vessel and the flow speed at the center of the vessel, respectively. In Fig. 3.7, the mean Doppler shift for laminar flow is shown with and without multiple-scattering effects included using Eqs. 3.33 and 3.32, respectively. The multiple scattering gives rise to a bias at the proximal end of the

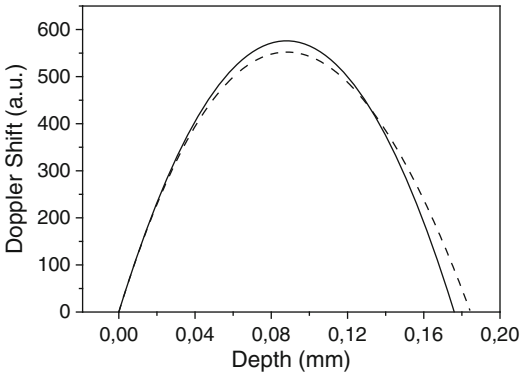

Fig. 3.7 The mean Doppler shift for laminar flow is shown with (*dashed*) and without (*solid*) multiple-scattering effects included using Eqs. 4.33 and 4.32, respectively ($\lambda_0 = 832$ nm, $\varepsilon = 80°$, $a = 88$ μm [56]; $\mu_s = 150\ \text{mm}^{-1}$, $\theta_{\text{rms}} = 0.141$ rad. [59]; $n = 1.38$ [91])

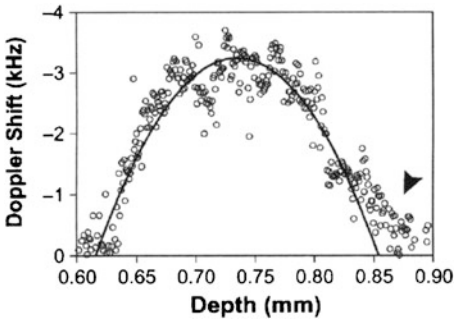

Fig. 3.8 Measurement of depth-resolved retinal flow profile taken (From Ref. [56]). The *arrow* indicates the effect of multiple scattering

profile, which is in qualitative agreement with ODT measurements of a depth-resolved retinal flow profile obtained by Yazdanfar et al. [56] and shown in Fig. 3.8. Typical scattering parameters for blood [59] are used in Fig. 3.7 together with ODT system parameters and vessel diameter from Ref. [56]. The bias increases with larger μ_s and θ_{rms} (or smaller anisotropy factor). No such bias was predicted by Lindmo et al. [59] because of their neglect of the stochastic distribution of wave vectors incident on the backscattering particle.

Furthermore, the dependence of the standard deviation of the Doppler-frequency spectrum on the scattering properties of the flowing medium is also obtained. Thus, the following approximate expression of the standard deviation of the Doppler-frequency spectrum valid for all values of $\mu_s z$ is obtained [58]:

$$\begin{aligned}\Delta f_T(d) &= \sqrt{\Delta f_D^2 + \Delta f_{D0}^2} \\ &= \sqrt{\frac{V^2(d) n^2 \sin^2 \varepsilon}{\lambda_0^2} \mu_s z \theta_{\text{rms}}^2 [2 + p(d)] + \Delta f_{D0}^2}\end{aligned} \tag{3.36}$$

where Δf_{D0} is the standard deviation of the Doppler-frequency spectrum in the absence of multiple scattering as reported previously in Ref. [55] and Δf_D is

the multiple-scattering contribution to the standard deviation of the ODT signal. The quantity $p(d)$ is given by [58]

$$p(d) = \frac{V_{\mathrm{rms}}^2(d) + \overline{V}(d)^2 - 4V(d)\overline{V}(d)}{V^2(d)}, \tag{3.37}$$

where $V_{\mathrm{rms}}(d)$ is the root-mean-square velocity of the flow along the propagation path to the probing depth z and is given by [58]

$$V_{\mathrm{rms}}(d) = \sqrt{\frac{1}{d}\int_0^d V^2(t)dt}. \tag{3.38}$$

The standard deviation increases with larger μ_s and θ_{rms} (or smaller anisotropy factor). As expected, a multiple-scattering contribution to the standard deviation of the ODT signal is obtained, which is identically zero for a constant velocity profile. This is in contrast to the work by Lindmo et al. [59], who arrived at a nonzero contribution from multiple scattering for this case.

3.4 Advanced Monte Carlo Simulation of OCT Systems

In the present section, the derivation of a Monte Carlo (MC) model capable of dealing with the heterodyne detection scheme. Adequate MC modeling may serve as a numerical phantom for further theoretical studies in cases where analytical modeling may be cumbersome.

It is important to note that the MC method only describes the transport of energy packets along straight lines and therefore the approach is incapable of describing coherent interactions of light. These energy packets are often referred to as photon packets or simply photons, and this terminology is adopted here. However, it should be emphasized that no underlying wave equation is guiding or governing these photons. Accordingly, any attempt to relate these to real quantum mechanical photons should be done with great care as argued in Ref. [60] commenting on a suggested approach of including diffraction effects into MC simulations [61, 62]. An MC photon packet represents a fraction of the total light energy, and for some applications, especially continuous wave, it may be useful to think of the path traveled by a photon as one possible path in which a fraction of the power flows. A collection of photon packets may then be perceived as constituting an intensity distribution due to an underlying field, and it can, accordingly, seem tempting to infer behavior known to apply to fields upon photon packets. Consider, as an example, that one wishes to determine whether the photon packets are able to enter an optical fiber. It can then seem intuitively correct to restrict the access of photons impinging on the fiber end to those which fall within the numerical aperture of the fiber. However, such an angular restriction may not be correct, because the individual photon packet does not carry information of the

entire field and its phase distribution. It is therefore impossible to determine whether a portion of the energy carried by a photon packet will enter the fiber due to a mode match between the fiber mode and the field underlying the collective intensity distribution of the photon packets. This discussion is treated in greater detail in Ref. [14].

With the above discussion of MC photons in mind, it may seem futile to investigate if MC simulation is applicable to estimate an OCT signal, which is the result of heterodyne mixing, and thus depends upon the coherence properties of the light. However, the problem may be reformulated to investigate whether or not the effect of the lack of coherence information in an MC simulation may be circumvented, or at least minimized. Others [63–66] have attempted to model similar optical geometries by interpreting the heterodyne process as a rejection process in which the detected photons must conform to a set of criteria on position and angle. Such a set of criteria is referred to as a detection scheme. However, these criteria were found by ad hoc considerations of the optical system, which may easily lead to incorrect results as exemplified above. Instead a mathematical derivation of the true criteria of the detection scheme will be given in the present section.

3.4.1 Theoretical Considerations

In the following, the EHF principle is used to derive an important result: an expression for the OCT signal depending on the intensity of the light only. This is obtained by calculating the mixing of the reference and sample beams in the plane conjugate to the plane in the sample probed by the system. The result is surprising, because the expression for the OCT signal depends on the coherence properties of the light [12]. However, it is shown that the formula used for calculating the OCT signal in this particular plane is mathematically identical to the result obtained in Ref. [12]. These results are valid for the, from a biomedical point of view, important case of a signal arising from a diffusely reflecting discontinuity embedded in a scattering sample. Note that this proves the viability of MC simulation to model the OCT technique, because it is shown that only intensity, and not field and phase, is necessary for this case.

The optical geometry of the sample arm is shown in Fig. 3.9, and it should be noted that the enclosed section corresponds to the geometry used for the EHF calculation in Sect. 3.2.2. An optical fiber end is positioned in the p-plane. The fiber emits a beam, which hits the collimating lens L1. The focusing lens L2 is positioned in the r-plane, and in this plane, the beam is a Gaussian beam with $1/e$ width, w_0, of the intensity. The beam is focused by L2 upon a diffusely reflecting discontinuity positioned at the depth z_f inside a scattering sample a distance d from L2. The sample is taken to be a slab infinite in the transverse direction. The part of the light that is reflected from the discontinuity propagates out through the sample, through lenses L2 and L1 to the optical fiber, where it is collected. The lenses L1 and L2 have the focal length f and are taken to be identical, perfect, and infinite in

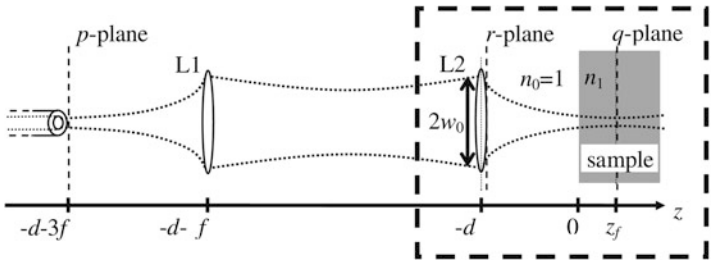

Fig. 3.9 Sample arm setup of the OCT system. The lenses L1 and L2 are considered to be identical, perfect, and have infinite radius. The setup is essentially a 4 F system (From Ref. [14])

radius. This means that the q- and p-planes are conjugate planes with magnification unity. The purpose of using the 4 F geometry is to have a physical representation of the conjugate plane to the probe plane. However, in Ref. [14] it is shown that the OCT signal term calculated from the conjugate plane is mathematically equivalent to the OCT signal calculated in the plane where the mixing physically takes place. Accordingly, the important result of Eq. 3.40 below is not restricted to the 4 F geometry. Hence, this proves the feasibility of using MC modeling in the analysis of OCT systems.

The OCT signal is produced by the mixing of the light from the reference and sample arms on the photodetector of the OCT system. Due to the symmetry of the system, in Sect. 3.2.2 the EHF prediction of the mixing between signal and reference beam was conveniently calculated at the r-plane. The mean square of the signal current $\langle i^2 \rangle$ is given by Eq. 3.9 and rewritten according to the notation in Fig. 3.9 to yield

$$\langle i^2(z) \rangle = 2\alpha^2 |\gamma(\tau)|^2 \mathrm{Re}\left[\iint \Gamma_S(\mathbf{p}_1, \mathbf{p}_2; z) \Gamma_R(\mathbf{p}_1, \mathbf{p}_2; z) d\mathbf{p}_1 d\mathbf{p}_2 \right] \equiv \Psi_r \langle i_0^2 \rangle, \quad (3.39)$$

where $\Gamma_R(\mathbf{r}_1, \mathbf{r}_2) = \langle U_R(\mathbf{r}_1) U_R{}^*(\mathbf{r}_2) \rangle = U_R(\mathbf{r}_1) U_R{}^*(\mathbf{r}_2)$ is the cross correlation of the scalar reference field, $\Gamma_S(\mathbf{r}_1, \mathbf{r}_2) = \langle U_S(\mathbf{r}_1) U_S{}^*(\mathbf{r}_2) \rangle$ is the cross correlation of the sample field, and $\mathbf{r}_1$ and $\mathbf{r}_2$ are vectors in the r-plane; see Fig. 3.9. Ψ_r is the heterodyne efficiency factor (defined in Eq. 3.17; subscript r refers to it being calculated in the r-plane), which quantifies the reduction in signal due to scattering, and $\langle i_0{}^2 \rangle$ is the OCT signal current in the absence of scattering.

It is important to note that by using the EHF principle, the investigation is limited to the paraxial regime as discussed in Sect. 3.2.1. In addition, most tissues are highly forward scattering in the near-infrared regime in which most OCT systems operate. It is assumed that the coherence length of the light source is short enough that signal powers from other reflections than the probed discontinuity are negligible. On the other hand, the coherence length is assumed long enough so that the temporal distortion of the sample field, or the path-length distribution of the reflected photons, is assumed negligible compared to the coherence length of the

light source. Assuming that the optical path length of the reference beam and sample beam reflected from the discontinuity are perfectly matched, then $\gamma(\tau) \approx 1$. To obtain the best comparison with the EHF model, the MC model presented in this section adopts this approximation.

The approximation of $\gamma(\tau) \approx 1$ is a justified approximation for highly forward scattering tissues [9]. However, it does render the EHF model unsuitable to investigate the effect of scattering on the axial resolution of an OCT system in general, because the coherence gate due to the limited coherence length of the light source is not incorporated. Others have suggested using MC simulation and the total optical path length traveled by a photon packet to determine the influence of the coherence gate [10, 29, 66]. While this may very well be a valid approach, it is clear from the above discussion of photon packets and coherence that, how intuitively correct it may seem, this may not be the case. However, no efforts have been published to establish the meaning of a photon packet in such a temporal mixing of fields, so future work is required to establish such a relation. It is the intention that the MC model of the OCT signal presented in this chapter may be instrumental in such studies.

The OCT signal depends upon the lateral cross correlation of the light from the scattering sample, as indicated by Eq. 3.17, and the lateral coherence length ρ_0 of the sample field in the r-plane for a single layer in front of the discontinuity is given by Eq. 3.21. With a nonzero lateral coherence length, ρ_0, it is seen that the OCT signal depends heavily upon the coherence properties of the field from the sample. As discussed above, an MC simulation does not describe the spatial coherence properties of light, and thus a direct simulation of Eq. 3.39 is not possible. As in Sect. 3.2.2, it is assumed that the discontinuity is diffusely reflecting, and this infers that the lateral coherence will be zero immediately after reflection. The motivation for envisioning the system geometry considered in Sect. 3.2.2 as part of a 4 F setup is to obtain a conjugate plane to the q-plane, here the p-plane; see Fig. 3.9. Through the conjugate relation, it is given that, in the absence of scattering, the lateral coherence length in the p-plane will also be zero. Hence, the sample field will be delta-correlated [20] and the OCT signal will only depend upon the intensities of the reference and sample field. In Appendix B of Ref. [14], it is shown that within the paraxial regime, the sample field is delta-correlated even in the presence of scattering. It is also shown that the heterodyne efficiency factor calculated in the p-plane Ψ_p is mathematically identical to the heterodyne efficiency factor calculated in the r-plane, so that

$$\Psi_p = \frac{\langle i^2 \rangle}{\langle i_0^2 \rangle} = \frac{\int I_R(\mathbf{p}) \langle I_S(\mathbf{p}) \rangle d^2\mathbf{p}}{\int I_R(\mathbf{p}) \langle I_{S0}(\mathbf{p}) \rangle d^2\mathbf{p}} = \Psi_r, \tag{3.40}$$

where I_R is the intensity at the reference beam and I_S, I_{S0} are the received intensities of the sample beam with and without scattering, respectively. The quantity $\mathbf{p}$ is

a vector in the p-plane; see Fig. 3.9. Equation 3.40 shows the viability of applying an MC simulation to an OCT system provided a good estimate of the intensity distribution of the sample field is achieved. This requires a method to simulate a focused Gaussian beam, and a method for modeling such a beam using MC simulation is discussed in Ref. [14]. Note that the identity proven in Eq. 3.40 is only strictly valid within the approximations of the EHF principle and thus also within the paraxial regime. However, for geometries with scattering that is not highly forward, directed coherence effects are expected to be of even less importance, and thus Eq. 3.40 should at least be a good first approximation even when the paraxial approximation is not strictly valid.

3.4.2 Monte Carlo Simulation of the OCT Signal

In Sect. 3.4.1, it is shown that the heterodyne efficiency factor of the OCT signal may be found using the knowledge of the intensity distributions of the sample and reference fields in the p-plane (see Fig. 3.9), where the fiber end is situated:

$$\Psi_p = \frac{\int I_R(\mathbf{p})\langle I_S(\mathbf{p})\rangle d^2\mathbf{p}}{\int I_R(\mathbf{p})\langle I_{S0}(\mathbf{p})\rangle d^2\mathbf{p}}. \tag{3.41}$$

In the EHF principle, the effect of a scattering medium is treated as a random phase distortion added to the deterministic phase of the light as it propagates through the medium. In the derivation of Eq. 3.41 (see also Appendix B of Ref. [14]), it is necessary to assume that the phase distortion added to the light propagating towards the discontinuity is statistically independent from the phase distortion added to the light propagating away from the discontinuity. It is important to note that this assumption is inherently fulfilled by MC methods such as that used by the MCML computer code [67]: a photon is traced through a dynamic medium in the sense that the distance to the next scattering event and scattering angle is a random variable independent upon the past of the photon. Hence, after each stochastic event, the photon experiences a different realization of the sample. Therefore, an ensemble averaging over the stochastic sample in Eq. 3.41 is carried out through a single simulation. Moreover, to also obtain an averaging in the modeling of the diffusely reflecting discontinuity, each reflected photon must experience a new realization of the discontinuity. Thus, the macroscopic intensity distribution of a Lambertian emitter [20] to sample the reflected angle is used

$$I_r(\theta_r) = I_T \cos\theta_r. \tag{3.42}$$

Here I_T is reflected intensity at $\theta_r = 0$ and θ_r is the reflected angle. By following the method outlined by Prahl et al. [68] of sampling a physical quantity using a computer-generated pseudorandom numbers, the following relations are obtained:

$$\theta_r = \arcsin(\xi), \tag{3.43}$$

$$\varphi_r = 2\pi\xi, \tag{3.44}$$

where φ_r is the azimuthal angle of the reflected photon and ξ and ζ are both random numbers uniformly distributed between 0 and 1.

Accordingly, the method of simulating the OCT signal is carried out as follows. The MC photon packet is launched from the focusing lens in the r-plane (see Fig. 3.9), using the focusing method (new hyperboloid method, Ref. [14]). The interfacing with specular surfaces, such as the sample surface and the propagation through the scattering medium, is carried out using the MCML computer code. When a photon packet is reflected off the diffusely reflecting discontinuity,[1] Eqs. 3.43 and 3.44 are used to determine the direction of the photon after reflection. As a photon exits the sample after interaction with the discontinuity, its position and angle are used to calculate its position in the p-plane after propagation through the 4 F system. To evaluate Eq. 3.41 numerically, consider that the mth photon packet exiting the medium contributes to the intensity at the point p_m in the p-plane by the amount

$$I_{S,m} \propto \frac{w_m}{\Delta p^2}, \tag{3.45}$$

where w_m is the energy, or weight, carried by the photon packet and Δp^2 is a differential area around p_m. Using this and Eq. 3.41, the MC estimated heterodyne efficiency factor Ψ_{MC} is then given by

$$\Psi_{\mathrm{MC}} = \frac{\sum_m^M I_R(p_m) I_{S,m} \Delta p^2}{\langle i_0^2 \rangle} = \frac{\sum_m^M I_R(p_m) W_m}{\langle i_0^2 \rangle}, \tag{3.46}$$

where $I_R(p)$ is the intensity distribution of the reference beam in the p-plane, and it is noted that the reference beam has a Gaussian intensity distribution of width w_f in the p-plane. The signal in the absence of scattering $\langle {i_0}^2 \rangle$ may be either simulated or calculated. The latter is straightforward, because with the conjugate relationship between the p- and q-plane, the intensity distribution of the sample beam will be identical to that of the reference beam in the absence of scattering.

[1] The reflection can also be treated as bulk backscattering; see, e.g., Ref. [28].

Equation 3.46 reveals the important detection criterion of the MC simulation of the OCT signal: a photon must hit the p-plane within the extent of the reference beam. While detection schemes of previously published MC models of OCT also incorporate that photons must hit the detector, the key element of this detection scheme is the analytically derived size and necessary position in the p-plane. Furthermore, contrary to these schemes, the model does not incorporate an angular criterion that a photon packet must fulfill in order to contribute to the signal. It may seem counterintuitive that photon packets contribute to the desired signal without penalty regardless of the angle of incidence upon the fiber in the p-plane. However, as demonstrated in Ref. [14], the inclusion of an angular criterion related to the angular extent of the incident beam, or equivalently the numerical aperture of the fiber, yields incorrect results.

3.4.3 Validation

3.4.3.1 Comparison to Experimental Data

The MC model has been verified by comparison to experimental data. In Ref. [12], an experimental setup is described and from this experimental data are obtained. The sample is an aqueous (refractive index 1.33) solution of microspheres (refractive index 1.59; diameter 2.04 μm). The experiment is carried out with the following parameters: source center wavelength $\lambda = 814$ nm, anisotropy $g = 0.929$ (calculated from Mie theory [45] using the particle diameter and refractive index), cuvette thickness $z = 0.5$ mm, focal length $f = 16$ mm, and beam radius $w_0 = 0.125$ mm. Hence, the probe depth remains fixed at $z = 0.5$ mm, and then the scattering coefficient is varied by changing the particle concentration.

From the experimental data, the heterodyne efficiency Ψ factor is derived. The result is plotted in Fig. 3.10 showing Ψ as a function of the scattering coefficient for the above parameters. The measurements are shown as open circles (○) connected with a straight dashed line. The MC data is shown as stars (*) connected with a solid line. For reference, the single-scatter case is plotted as the dotted line. As indicated in Fig. 3.10, good agreement between experiments and the MC model is obtained.

3.4.3.2 Beam Geometries for Numerical Comparison

A set of beam geometries has been selected for numerical comparison between the EHF model and the MC model. These geometries are selected so that the two approaches are compared for different degrees of focusing and distances between the lens L2 and the sample. The selected cases are listed in Table 3.1 and are referred to as cases 1 through 4, respectively.

For all cases the mean refractive index of the sample before the discontinuity and the surroundings are assumed to be matched so that $n_0 = n_1 = 1$. The subject of the investigation is the effect of scattering on the OCT signal. A difference in the refractive index between the sample and the surroundings will impose a Snell's law refraction at the interface, which in turn imposes a focus distortion not treated in the paraxial approximation ($\sin\theta \approx \theta$) and thus not described by the EHF model.

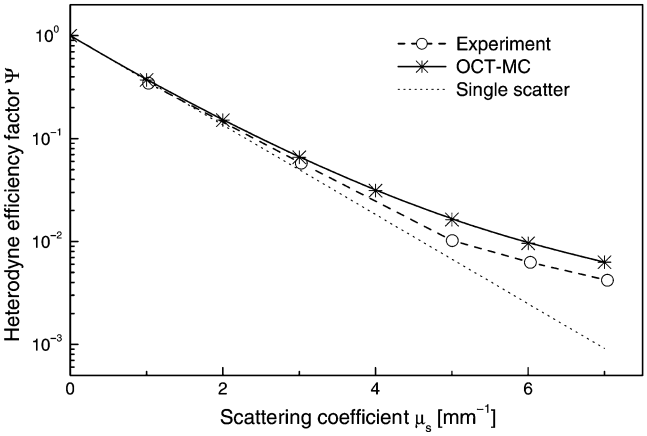

Fig. 3.10 Heterodyne efficiency factor as a function of the scattering coefficient for an aqueous solution of microspheres. Experimental data: *open circles* (○) connected with *dashed line*. MC simulations: stars (*) connected with *solid line*. *Dotted line* shows single-scatter regime for reference. Parameters used: source center wavelength $\lambda = 814$ nm, anisotropy $g = 0.929$ (calculated from the particle diameter and refractive index), cuvette thickness $z = 0.5$ mm, focal length $f = 16$ mm, and beam radius $w_0 = 0.125$ mm

Table 3.1 Beam geometries for the four cases

Case number	f [mm]	d [mm]	z [mm]	w_0 [mm]	w_0/f
1	16.0	15.5	0.5	0.125	0.008
2	8	7.5	0.5	0.4	0.05
3	0.5	0.0	0.5	0.125	0.25
4	16.0	15.0	1.0	4	0.25

Such a distortion will be difficult to separate from the effects of scattering and is thus omitted here. As discussed in Ref. [14], there is only a severe distortion for very tightly focused beams.

In all cases discussed in the following, the wavelength of the light is chosen to be 814 nm, which is one relevant wavelength for biomedical applications of OCT. The sample is assumed to exhibit scattering described by a Gaussian scattering function (see, e.g., Chap. 13 in Ref. [37]). The motivation for this choice is to enable comparison to analytical models of the propagation of Gaussian beams in random media [41] and the OCT signal (see Sect. 3.2.2), which both applies the Gaussian scattering function. The comparisons presented here are carried out for different degrees of scattering and for two relevant values of the asymmetry parameter in tissue [44]: very highly forward scattering ($g = 0.99$) and highly forward scattering ($g = 0.92$). The value $g = 0.92$ was the value of the asymmetry factor in the experiments performed to validate the EHF model by Thrane et al. [12]. With these two cases, the two approaches are compared for a sample geometry where the paraxial approximation is well satisfied

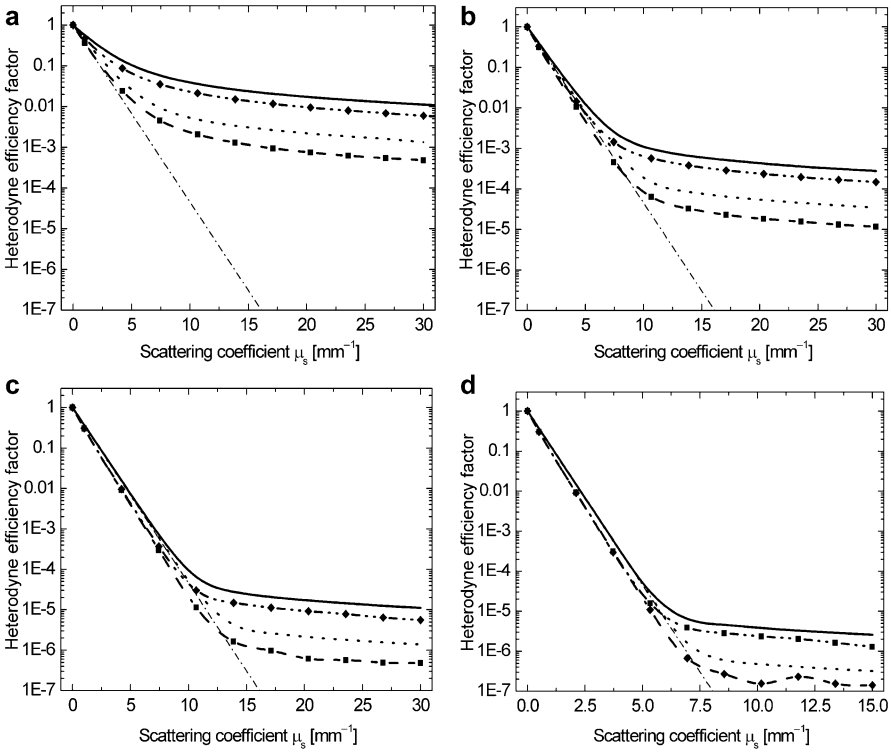

Fig. 3.11 Heterodyne efficiency factors estimated using, respectively, the EHF model and the MC method for two cases of g. (**a–d**) Show the estimated values for geometries 1, 2, 3, and 4 in Table 4.1, respectively. The *solid line* and *dotted line* curves are the results of the EHF model for $g = 0.99$ and $g = 0.92$, respectively. *Dash-dot-dot* and *dashed curves* are the results of the MC simulations for $g = 0.99$ and $g = 0.92$, respectively. *Diamonds* (◆) and *squares* (■) mark the actual data points obtained by the MC simulation method. For comparison, the exponential reduction in signal due to scattering obtained by a single-scatter model is shown as a *dash-dot curve*

and for a sample geometry, which is close to the limit of the paraxial approximation. Accordingly, it is expected that the best agreement will be found for $g = 0.99$.

3.4.3.3 Comparison to Analytical Model

In Fig. 3.11, Ψ is plotted for cases 1 through 4 as a function of the scattering coefficient μ_s, and for reference the case of single backscattering, i.e., $\Psi_{\text{single}} = \exp(-2\mu_s z)$, has been included. Three important observations may be made from Fig. 3.11. Firstly, fine agreement between the MC method and the EHF model for the four cases tested is observed. Thus, these plots are considered the validation of the MC model. Alternatively, the MC results can be considered as the confirmation of the EHF results. Secondly, it is inferred that the OCT signal for high optical depths is a result of multiple-scattering effects in agreement with Sect. 3.2.2. This is seen by

comparing the single-scattering curve to the plots of the MC and EHF. Finally, an important result of Sect. 3.2.2 was the inclusion of the so-called shower-curtain effect [18]. It is an effect caused by multiple scattering and thus plays an important role in calculating the OCT signal as the optical depth increases. Omitting this effect leads to an underestimation of the OCT signal of several orders of magnitude. Due to the good agreement between the EHF model (with the shower-curtain effect included) and the MC model, the important result that the MC model inherently takes the effect into account is obtained.

For cases where the approximation of the EHF model is well satisfied, the observed deviation between the EHF and MC models is likely to be caused by coherence effects in the intensity distribution of the sample field. Apparently, from Fig. 3.11, the lack of coherence information leads to an underestimation of Ψ, but the specific cause for this has yet to be determined. Ψ is by definition unity in the absence of scattering, and for large optical depths, coherence effects are expected to be negligible. Accordingly, the two models are expected to agree for small and large values of the optical depth of the discontinuity, whereas some deviation is to be expected in the intermediate region. As a highly forward scattering event perturbs the field only to a small degree, it is expected to distort coherence effects less than a more isotropic scattering case. In order to plot the relative deviation as a function of the effective distortion of the coherence, the ratio $\Psi_{\mathrm{EHF}}/\ \Psi_{\mathrm{MC}}$ is considered as a function of the transport reduced optical depth of the discontinuity given by

$$S_{tr} = \mu_s z_f (1 - g). \tag{3.47}$$

The relative difference between the EHF model and the MC method behaves, qualitatively, identical as a function of s_{tr} independent of beam geometry and g. This is illustrated in Fig. 3.12 for cases 2 ($g = 0.92$ and 0.99), 3 ($g = 0.92$), and 4 ($g = 0.92$), respectively. The difference between the two approaches increases as a function of s_{tr} until $s_{tr} \approx 0.5$ after which it levels off. This is mainly attributed to the coherence effects in the intensity distribution discussed above. The more abrupt behavior of the curve for geometry 4 is attributed to a higher numerical uncertainty in the case, caused by a more tightly focused beam. According to the detection scheme applied in these simulations, this implies that fewer photons will contribute to the signal resulting in an increased variance. Therefore, due to the good agreement between the results of the EHF model and MC simulations borne out in Figs. 3.11 and 3.12, it is concluded that the MC simulation presented in this section is a viable method of simulating the heterodyne efficiency factor of an OCT signal.

3.5 Applications of Modeling in OCT

The interpretation of OCT images displaying structural information only may be a difficult task, i.e., making adequate assessment of the imaged sample or tissue.

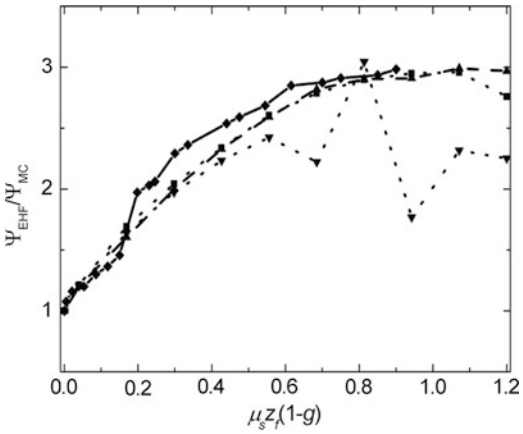

Fig. 3.12 The relative numerical difference between the results of the EHF model and the MC model from Fig. 4.11 for a representative selection of the considered geometries. The ratio Ψ_{EHF}/Ψ_{MC} is plotted for case 2 and $g = 0.99$ with symbols (♦) and *solid curve*, for case 2 and $g = 0.92$ with symbols (■) and *dash-dot-dot curve*, for case 3 and $g = 0.92$ with symbols (▼) and *dashed curve*, and for case 4 and $g = 0.92$ with symbols (•) and *dotted curve* (From Ref. [14])

An OCT signal, i.e., the detected envelope function of the A-scan, measured at a given position in a nonabsorbing scattering medium is the result of the amount of light reflected at the given position and the attenuation due to scattering when the light propagates through the scattering medium. Therefore, in order to make images, which give a direct measure of the amount of light reflected at a given position, it is necessary to be able to separate reflection and scattering effects; see, e.g., Refs. [47, 69] for details on the so-called true-reflection OCT imaging algorithm. Such kind of post processing is similar to the correction for attenuation well known in ultrasonic imaging. In that field, a mathematical model describing the relationship between the received signal and the two main acoustic parameters, backscatter and attenuation, has been considered [70]. The model has then been used to guide the derivation of a processing technique with the aim of obtaining ultrasonic images that faithfully represents one acoustic parameter, such as backscatter [70].

Extraction of optical scattering parameters from OCT images is a method to obtain more quantitative information from these images in order to improve the diagnostics (see, e.g., Ref. [71]), i.e., an alternative method of functional imaging. Accordingly, one may envisage a novel functional imaging method where, in addition to tissue morphology, parameters such as the scattering parameters, g and/or μ_s, or mean refractive index is obtained.

In the following, the viability of the suggested approach in OCT is briefly overviewed. First, a method based on the modeling in Sect. 3.2 is discussed showing that the method may be expanded to more than one layer and that optical scattering properties may be successfully extracted. Finally, some examples highlighting the extraction of optical scattering properties in tissues in vitro and in vivo are given.

3.5.1 Extracting Optical Scattering Properties from an MC-Simulated Heterogeneous Multilayered Sample

It was shown in Sect. 3.2.2 that the mean square heterodyne signal current for light reflected at depth z in the tissue may be expressed as $\langle i^2(z)\rangle = \langle i^2(z)\rangle_0 \Psi(z)$, where $\langle i^2(z)\rangle_0$ is the mean square heterodyne signal current in the absence of scattering and $\Psi(z)$ is the heterodyne efficiency factor, which includes all of the scattering effects. The maximum of the envelope of the measured interference signal corresponds to $[\langle i^2(z)\rangle]^{1/2}$. In practice, μ_s and θ_{rms} may be obtained by fitting the expression for $[\langle i^2(z)\rangle]^{1/2}$ to a measured (or simulated) depth scan of the homogeneous backscattering tissue. It is important to note that in addition to the system parameters λ, f, and w_0, knowledge about the mean index of refraction n of the scattering medium is necessary in order to perform the fitting. Otherwise, the refractive index should be fitted as well as in Ref. [72].

For OCT images of tissue, a multilayered analytical OCT model with multiple-scattering effects included is essential in order to extract optical scattering parameters. In this section, details are given of a method for multilayered extraction of optical scattering parameters [69] by expanding the OCT model developed in Sect. 3.2. Thus, the model makes it straightforward to model OCT imaging in heterogeneous multilayered tissue together with different focusing conditions, i.e., dynamic focusing or fixed focus position.

3.5.1.1 Expressions for Two-Layered Medium

The analytical expressions for the OCT signal of the two layers are obtained from the general expression given by Eq. 3.18. Note that the OCT signal is the root-mean-square (rms) heterodyne signal current $\langle i^2(z)\rangle^{1/2}$. In the case of dynamic focusing, $\langle i^2\rangle_0$ is a constant proportional to the effective backscattering cross section of the sample. For the first layer, characterized by the optical parameters μ_{s1}, θ_{rms1}, and n_1, μ_s and z in Eq. 3.18 are replaced by μ_{s1} and z_1, respectively, where z_1 is the probing depth in the first layer. The lateral coherence length $\rho_{01}(z)$ is then given by [69]

$$\rho_{01}(z_1) = \sqrt{\frac{3}{\mu_{s1} z_1}} \frac{\lambda}{\pi \theta_{\text{rms1}}} \left[\frac{n_1 f}{z_1}\right]. \tag{3.48}$$

For the second layer, characterized by μ_{s2}, θ_{rms2}, and n_2, z and $\mu_s z$ in Eq. 3.18 are replaced by z_2 and $\mu_{s1}\Delta_1 + \mu_{s2} z_2$, respectively, where Δ_1 is the thickness of the first layer and z_2 is the probing depth in the second layer. Furthermore, for the second layer, $\rho_{02}(z)$ is given by [69]

$$\rho_{02}(z_2) = \frac{\sqrt{3}}{\pi} \sqrt{\frac{\left\{\lambda n_2 \Delta_1 + \lambda n_1 \left[z_2 + n_2\left(f - \frac{\Delta_1}{n_1} - \frac{z_2}{n_2}\right)\right]\right\}^2}{n_2^2 \Delta_1 \left(\Delta_1^2 + 3\Delta_1 z_2 + 3z_2^2\right)\theta_{\text{rms1}}^2 \mu_{s1} + n_1^2 z_2^3 \theta_{\text{rms2}}^2 \mu_{s2}}}. \tag{3.49}$$

Table 3.2 The input parameters of the MC simulation together with the extracted parameters obtained by using the EHF model and the relative difference (%). Leave-one-out cross-validation [92] with respect to the MC data points has been used to estimate the standard deviations

Layer	MC input μ_s [mm^{-1}]	Extracted μ_s [mm^{-1}]	Rel. diff. [%]	MC input g-	Extracted g-	Rel. diff. [%]
1	5.000	4.98 ± 0.05	−0.4	0.9900	0.974 ± 0.007	−1.6
2	4.000	4.4 ± 0.1	10	0.9200	0.940 ± 0.003	2.2
2	6.000	6.3 ± 0.1	5.0	0.9200	0.893 ± 0.003	−2.9
2	8.000	8.2 ± 0.1	2.5	0.9200	0.874 ± 0.005	−5.0
2	10.00	9.9 ± 0.2	−1.0	0.9200	0.864 ± 0.006	−6.1

3.5.1.2 Extracting the Optical Scattering Parameters from Layered MC Model

The MC model presented in Sect. 3.3 is used as a numerical phantom. Hence, the versatility of the MC model is demonstrated; for example, it may be used to investigate the performance of the EHF model for sample geometries difficult to produce in the laboratory. By using this model, depth scans of layered scattering structures (tissue) may be obtained. In the present context, a layer is here defined as a plane-parallel homogeneous region characterized by a scattering coefficient μ_s, an anisotropy factor g, and an index of refraction n.

Next the two-layer EHF expression for the OCT signal is fitted to the MC-simulated signal, the optical scattering properties μ_s and g of each of the two layers are extracted, and the MC input values are compared with them. Strictly speaking, the extracted g is the effective anisotropy factor given by the cosine of θ_{rms}, where θ_{rms} is the rms scattering angle defined as the half-width at $1/e$ maximum of a Gaussian curve fit to the main frontal lobe of the scattering phase function of the sample [12]. Because the scattering phase function used in the MC OCT model is also Gaussian, the extracted g values can be directly compared with the MC input g values. The system parameters in this case are $\lambda = 800$ nm, $w_o = 0.4$ mm, and $f = 8.0$ mm. The first layer is 0.3 mm thick (Δ_1) with $\mu_{s1} = 5.0\ mm^{-1}$ and $g_1 = 0.99$. The second layer is 0.9 mm thick with $\mu_{s2} = 10.0\ mm^{-1}$ and $g_2 = 0.92$. Without the loss of generality, the refractive indices of the sample and the surroundings are matched and equal unity.

Table 3.2 shows the main result by comparing the input optical scattering parameters used in the MC simulation to the extracted values including the relative difference. The absolute relative differences between the extracted mean values and the values used in the MC simulation follow a kind of structured pattern with increasing values of μ_{s2}, and the "true" values are not contained within the estimated standard deviations. This observation is an indication of a bias between the EHF model and the MC simulations. On the other hand, the small relative differences demonstrate the capability of the EHF OCT model to extract optical scattering parameters from multilayered tissue. In general, the index of refraction of each layer may also be extracted, but that is outside the scope of the present analysis.

Notice that μ_s and g_{eff} can only be separated if the optical depth of each layer is sufficiently large that multiple scattering occurs. In case the optical depth is too small, only single scattering occurs and therefore only μ_s can be extracted. For large optical depths, i.e., totally diffused light, the EHF model predicts the OCT signal to be determined by the reduced scattering coefficient, and hence, μ_s and g_{eff} cannot be separated for this case (cf. Eq. 3.22, Sect. 3.2.2.1).

3.5.2 Extraction of Optical Scattering Properties from Tissues

As mentioned at the beginning of the present section, attenuation compensation is widely accepted within ultrasonic imaging. Therefore, it has also been among the first attempts to improve on OCT imagery. In fact, attenuation compensation is a method to remove the attenuation caused by scattering in OCT images. This should improve the diagnostic capabilities due to a better differentiation of different tissue types. There have been few attempts to do attenuation compensation in OCT images of tissue by using the single-scattering OCT model [73]. However, due to the fact that multiple-scattered photons contribute to the OCT signal, the single-scattering OCT model is insufficient for this purpose. Attenuation compensation was verified on a single-layer phantom by using an OCT model taking multiple-scattering effects into account [74].

The optical scattering properties themselves, however, also contain information about the tissue. For example, cell mitochondria are affected or changed in several malignant conditions, and through these changes the scattering changes. Conversely, provided that information about the scattering properties can be obtained with good accuracy and good (high) spatial resolution, new diagnostics can be performed [71]. This fact is one important motivation for attempting to extract optical scattering properties in order to improve the diagnostic potential of OCT.

By using the single-scattering OCT model [2], studies have been carried out with the aim to extract only the scattering coefficient μ_s from OCT images of tissue. This approach was applied in various important applications. For example, glucose monitoring was investigated by using the single-scatter approach [75] and expanded to include phase-sensitive OCT [76]. The anisotropy factor g may also be extracted as demonstrated by Kodach et al. [77]. In their study, they showed that monitoring this parameter might offer a contrast mechanism for changes in back-scattering and, hence, indicate morphological changes. Determining optical scattering properties of blood is also of high importance. Faber et al. [78, 79] demonstrated that the optical absorption spectra of oxygenated and deoxygenated hemoglobin, corrected for optical scattering, may be obtained by using spectral OCT. The underlying OCT modeling was based on a single-scattering approach.

Important contributions have been made in in vitro characterization of atherosclerotic plaque by several groups. Studying in vitro samples with various stages of atherosclerotic plaque, van der Meer et al. extracted the optical scattering coefficient [80]. Although the model applied was based on a single-scattering model, their findings provide important data on the optical scattering coefficient of these plaques. A larger study also demonstrated that the scattering coefficient may provide valuable,

additional information, thus improving diagnosis [81]. Some data for the scattering coefficients reported in [81] correlate well with other findings, but some data showed significant deviations: these deviations can, however, be explained by different sample handling and fit to different models, respectively; see also below. In their review paper, Kubo et al. [82] provided an excellent overview on sample handling, extraction of optical parameters, and its diagnostic potential in the clinic. Because OCT is established in cardiology, e.g., stent deployment, such added diagnostic potential seems highly feasible.

Extraction of optical properties has also been investigated targeting other diseases. Quantitative analysis of rectal cancer by spectral domain OCT was demonstrated [83]. Their study involved 16 samples in vitro comprising 1,000 measurement: one half benign and one half malignant. In particular, their results showed that the quantitative analysis of rectal tissue can be used as a promising diagnostic criterion of early rectal cancer. This is noteworthy because early diagnosis has great value for clinical application and earlier onset of treatment. Oral mucosal tissue has also been investigated [84] by using swept source OCT showing promise for early diagnosis. Both studies were carried out under the assumption that single scattering was sufficient to describe the light–tissue interaction. Woolliams and Tomlins [85] claimed that multiple scattering is not affecting the OCT signal at longer wavelengths, but this seems to have been dismissed by several other reports showing clear evidence of the opposite fact. Their statement [85] might, however, be correct with respect to their specific system (data fitting) or application (also mentioned by the authors [85]). Note that for superficial lesions, multiple scattering might be negligible; hence for such applications simplified modeling may suffice.

In general, multiple scattering is impacting the formation of the OCT signal (A-scan). Provided an OCT model is used that takes into account multiple scattering, both μ_s and the anisotropy factor g may be extracted. Extraction for a two-layer geometry has been carried out [69, 86], where both μ_s and g were obtained for each (tissue) layer. In Ref. [69] MC simulations were used as numerical phantom as discussed in detail in the previous subsection.

Lee et al. [28] compared single-scattering and multiple-scattering models for extracting optical scattering properties, and using calibrated scattering phantoms, the validity of the single-scattering and multiple-scattering models for both highly scattering and weakly scattering media was investigated. They showed, with a proper correction for the confocal properties of the sample arm, both models are appropriate to extract the scattering coefficients of weakly scattering media. For highly scattering media, the multiple scattering must be taken into account, and the multiple-scattering model provides much higher accuracy. In their study, they applied the EHF model described in this chapter and in Ref. [12] modeling the multiple scattering. They also investigated the scattering properties of in vitro rat liver and in vivo human skin and concluded that the EHF model is useful for quantitatively characterizing tissue scattering.

A number of in vitro studies have been reported. The characterization of atherosclerotic plaque using a single, multiple-scattering layer model has been reported [87]. The method of extracting the optical scattering properties was

verified using well-controlled and calibrated, single-layer tissue-like phantoms. The study provided the optical scattering properties in 1,300 nm range for lesions in different stages including the anisotropy parameter. Based on the extracted parameters, normal tissue could be separated from malignant tissue. It should be noted that some discrepancies occur between the reported values for the scattering coefficients in Refs. [87, 80]. Possible explanations for the differences may be due to different sample handling and fit to different models. The results reported in both Refs. [87, 80] are encouraging although further studies are required to fully establish these criteria and thereby demonstrate the feasibility of the method in this particular area.

The EHF model, as described in the present chapter and Ref. [12], has been validated and expanded by other groups. Most notably, the work of Kuo et al. [88] concluded that multiple scattering had to be taken into account in the assessment of arterial characteristics in human atherosclerosis. Moreover, they expanded the extraction to also include polarization parameters, thus establishing a refined criterion as compared to previous work; see, e.g., [87].

In Ref. [13], an excellent study comprising rigorous application of the RTE modeling (small-angle approximation) in the extraction of optical parameters is presented. First, the authors verified their modeling on a well-controlled tissue-like phantom. By estimating covariance and confidence regions for the extracted optical properties, they point to specific regimes of the OCT signal decay where extraction is likely to fail. These regimes depend on both the optical properties and sample beam geometry. Hence, their findings provide important insight of how to optimize the OCT system for a specific application. The authors applied their method to cervical tissue (cervical dysplasia 2–3 and leukoplakia). In their in vitro investigation, they demonstrated that cervical dysplasia 2–3 and leukoplakia could be distinguished on the basis of the extracted optical scattering properties. Hence, their excellent contribution should be an encouragement for expanding to other clinical applications and finally in vivo applications.

In vivo studies are sparse; however, Knüttel et al. [72] took the approach of extracting optical scattering properties using the EHF model [12] and refractive index aiming at relating the effects of skin hydration to the optical properties extracted from OCT images. Their investigation showed the applicability of the approach and the potential in dermatology to provide new diagnostic information.

3.6 Summary

Advanced models for describing the light–tissue interactions in optical coherence tomography (OCT) systems have been reviewed. Firstly, an analytical model based on the extended Huygens–Fresnel (EHF) principle is presented valid for the single- and multiple-scattering regimes simultaneously. Because the model is based on the general *ABCD*-matrix formalism, it is applicable to any sample arm geometry, and it leads to closed-form solutions for the OCT heterodyne signal. Expressions for

static and dynamic focusing were presented. Furthermore, expressions for the effects of multiple scattering on the detected OCT signal in Doppler OCT were presented and reasonable agreement with experimental data shown. Notice that the multiple-scattering EHF analysis presented here yields accurate analytical expressions for the OCT signal for a wide range of optical configurations that both are amenable to physical interpretation and are desirable for use in parametric studies for OCT system optimization.

From the EHF model a mathematical proof may be established showing that Monte Carlo (MC) simulations indeed may be used to model OCT system despite the fact that the MC model is restricted to the calculation of intensities and calculation of the OCT heterodyne signal involves the optical fields. Both the analytical and the numerical model compared favorably to experimental data. Moreover, good agreement between the analytical model and the MC simulations was found over a large range of optical scattering parameters and sample arm geometries.

Extraction of optical scattering parameters from OCT images is a method to obtain more quantitative information from these images in order to improve the diagnostics, i.e., an alternative method of functional imaging. Accordingly, one may envisage a novel functional imaging method where, in addition to tissue morphology, parameters such as the optical scattering parameters or mean refractive index are obtained. In addition, other functional parameters, such as polarization properties, can also be combined with the aforementioned scattering properties. The optical scattering properties themselves contain information about the tissue. For example, cell mitochondria are affected or changed in several malignant conditions, and through these changes the scattering changes. Conversely, provided that information about the scattering properties can be obtained with good accuracy and good (high) spatial resolution, new diagnostics can be performed. A survey highlighting important investigations aiming at bringing the modeling of the light–tissue interaction into OCT diagnostics was presented. The examples spanned theoretical/numerical in vitro and in vivo investigations. Although further work is needed, it seems that, in addition to or in combination with other functional imaging modalities, the extraction of optical scattering properties seems feasible and may ultimately improve OCT imagery and its diagnostic potential.

Appendix: Calculation of Γ_S

In the determination of the mutual coherence function Γ_S in Eq. 3.9, the EHF principle is applied in order to obtain a viable expression for $U_S(\mathbf{p};z)$, i.e., the reflected sample optical field. Using Eq. 3.2, $U_S(\mathbf{p};z)$ is related to the reflected sample field $U_B(\mathbf{r};z)$ in the probing plane, where $\mathbf{r}$ defines a two-dimensional vector in this plane:

$$U_S(\mathbf{p};z) = \int U_B(\mathbf{r};z)G(\mathbf{r},\mathbf{p};z)d\mathbf{r}. \tag{3.50}$$

Here $G(\mathbf{r},\mathbf{p};z)$ is Green's function response at $\mathbf{p}$ due to a point source at $\mathbf{r}$, which includes the effects of scattering in the intervening medium. Combining Eqs. 3.11 and 3.50 yields

$$\Gamma_S(\mathbf{p}_1,\mathbf{p}_2;z) = \iint \langle U_B(\mathbf{r}_1;z)U_B(\mathbf{r}_2;z)G(\mathbf{r}_1,\mathbf{p}_1;z)G^*(\mathbf{r}_2,\mathbf{p}_2;z)\rangle d\mathbf{r}_1 d\mathbf{r}_2, \quad (3.51)$$

where $\mathbf{r}_1$, $\mathbf{r}_2$ are associated two-dimensional vectors in the transverse plane. For simplicity in notation, the explicit dependence of the various quantities on z is omitted in the following.

If the forward propagated light is assumed to be statistically independent from the backscattered light, thereby neglecting coherent backscattering, the following relation holds:

$$\left\langle U_B(\mathbf{r}_1)U_B^*(\mathbf{r}_2)G(\mathbf{r}_1,\mathbf{p}_1)G^*(\mathbf{r}_2,\mathbf{p}_2)\right\rangle = \left\langle U_B(\mathbf{r}_1)U_B^*(\mathbf{r}_2)\right\rangle \langle G(\mathbf{r}_1,\mathbf{p}_1)G^*(\mathbf{r}_2,\mathbf{p}_2)\rangle. \quad (3.52)$$

If, furthermore, diffuse backscattering is assumed from the layer being probed, one gets [18, 89]

$$\left\langle U_B(\mathbf{r}_1)U_B^*(\mathbf{r}_2)\right\rangle = \frac{4\pi}{k^2}\delta(\mathbf{r}_1-\mathbf{r}_2)\langle I_B(\mathbf{r}_1)\rangle, \quad (3.53)$$

where $\delta(\mathbf{r})$ is the two-dimensional Dirac delta function and $I_B(\mathbf{r}_1)$ is the mean backscattered irradiance distribution in the plane of the discontinuity. Combining Eqs. 3.51, 3.52, and 3.53 and simplifying yields

$$\Gamma_S(\mathbf{p}_1,\mathbf{p}_2) = \frac{4\pi}{k^2}\int \langle I_B(\mathbf{r})\rangle \langle G(\mathbf{r},\mathbf{p}_1)G*(\mathbf{r},\mathbf{p}_2)\rangle d\mathbf{r}. \quad (3.54)$$

Using Eq. 3.3, the second term in the integral on the right-hand side of Eq. 3.54 may be written as

$$\langle G(\mathbf{r},\mathbf{p}_1)G^*(\mathbf{r},\mathbf{p}_2)\rangle = G_0(\mathbf{r},\mathbf{p}_1)G_0^*(\mathbf{r},\mathbf{p}_2)\Gamma_{pt}(\rho), \quad (3.55)$$

where $G_0(\mathbf{r},\mathbf{p})$ is Huygens–Fresnel Green's function when propagating from the probing plane to the lens plane and Γ_{pt} is the mutual coherence function of a point source located in the probing plane and observed in the lens plane given by

$$\Gamma_{pt} = \langle \exp[i\{\phi(\mathbf{p}_1)-\phi(\mathbf{p}_2)\}]\rangle. \quad (3.56)$$

The mutual coherence function Γ_{pt} contains the effects of the scattering inhomogeneities. Using Eq. 3.4, Green's function $G_0(\mathbf{r},\mathbf{p})$ is given by

$$G_0(\mathbf{r},\mathbf{p}) = -\frac{ik}{2\pi B_b}\exp\left[-\frac{ik}{2B_b}\left(A_b r^2 - 2\mathbf{r}\cdot\mathbf{p} + D_b p^2\right)\right], \tag{3.57}$$

where A_b, B_b, and D_b are the ray-matrix elements for back propagation to the lens plane. These quantities are given by $A_b = D = 1$, $B_b = B = d + z/n$ and $D_b = A = 1$ [39].

$\langle I_B(\mathbf{r})\rangle$ in (3.54) is simply related to the incident mean irradiance distribution $\langle I(\mathbf{r})\rangle$ in the probing layer dz around z by the following relation:

$$\langle I_B(\mathbf{r})\rangle = p_b \mu_s dz \langle I(\mathbf{r})\rangle \tag{3.58}$$

The EHF principle yields that the mean irradiance distribution is given by [39]

$$\langle I(\mathbf{r})\rangle = \left(\frac{k}{2\pi B}\right)^2 \int K(\rho)\exp\left\{\frac{ik}{B}\rho\cdot\mathbf{r}\right\}\Gamma_{pt}(\rho)d^2\rho, \tag{3.59}$$

where

$$K(\rho) = \int \exp\left\{-\frac{ikA}{B}\boldsymbol{\rho}\cdot\mathbf{P}\right\} U_{Si}(\mathbf{P} + \boldsymbol{\rho}/2)U_{Si}^*(\mathbf{P} - \boldsymbol{\rho}/2)d^2P, \tag{3.60}$$

and $\boldsymbol{\rho} = \mathbf{p}_1 - \mathbf{p}_2$. With the considered OCT setup focusing at depth z, $A = 1$ and $B = f$. The mutual coherence function Γ_{pt} can then be found to be [89]:

$$\Gamma_{pt} = \langle \exp\{i[\phi(\mathbf{p}_1) - \phi(\mathbf{p}_2)]\}\rangle = \exp\{-s[1 - b_\phi(\rho)]\}, \tag{3.61}$$

where it has been assumed that the phase ϕ is a normally distributed zero-mean random process. The quantity s is the phase variance, and $b_\phi(\rho)$ is the normalized phase autocorrelation function for a point source whose origin is at the probing depth z. It can be shown [90] that the phase variance is equal to the optical depth, $s = \mu_s z$. The normalized phase autocorrelation function $b_\phi(\rho)$ is given by [89]

$$b_\phi(\rho) = \frac{\int_0^L dz' \int_0^\infty \sigma(\theta; z')J_0(kp_s\theta)\theta d\theta}{\int_0^L dz' \int_0^\infty \sigma(\theta; z')\theta d\theta}, \tag{3.62}$$

where J_0 is the Bessel function of the first kind and of order zero, and

$$P_s = \frac{B_b(z')}{B_b}\rho, \tag{3.63}$$

where $B_b(z')$ is the B-matrix element for back propagation from the probing depth z to a distance z' and $\sigma(\theta; z')$ is the volume scattering or phase function with θ being the scattering angle. For the OCT geometry treated here $B_b(z') = z'/n$ for $0 \le z' \le z$, $L = d + z$, and $\sigma(\theta; z') = \sigma(\theta)$ for $0 \le z' \le z$, and zero otherwise. As described in Eq. 3.5, the phase function is modeled as a combination of a forward scattering term and a small isotropic term. The forward part is modeled here as a Gaussian volume scattering function, which in the small-angle approximation gives a phase function of the following form:

$$\sigma_1(\theta, z) = \exp\left[-\theta^2/\theta_0^2\right], \tag{3.64}$$

where $g = \langle \cos\theta \rangle \approx 1 - \langle\theta^2\rangle/2$, and $\theta_0 = \sqrt{\langle\theta^2\rangle} \approx \sqrt{2(1-g)}$. Substituting Eqs. 3.63 and 3.64 into Eq. 3.62 and performing the indicated integrations yield the following equation for the normalized phase autocorrelation function:

$$b_\phi(\rho) = \frac{\sqrt{\pi}}{2}\frac{\rho_\phi}{\rho}\mathrm{erf}\left(\rho/\rho_\phi\right)[1 - 2p_b], \tag{3.65}$$

where erf(·) denotes the error function and ρ_ϕ is the phase correlation length given by

$$\rho_\phi = \frac{\lambda}{\pi\sqrt{2(1-g)}}\left(1 + \frac{nd}{z}\right). \tag{3.66}$$

Hence, the mutual coherence function Γ_{pt} is given by Eq. 3.61 with $b_\phi(\rho)$ defined by Eq. 3.65. Thus, for specific values of both s and g, the mutual coherence-function is completely determined, and for a given value of the initial optical wave function U_{Si}, numerical results for the mean irradiance can be obtained directly from Eq. 3.59. Here U_{Si} is given by Eq. 3.7, and the following expression for the mean irradiance distribution is obtained at the probing depth z in the tissue:

$$\langle I(\mathbf{r})\rangle = \frac{P_S}{2\pi(f/kw_0)^2}\int_0^\infty \exp\left\{-x^2/4\right\} x J_0(ux)\Gamma_{pt}(xw_0)dx, \tag{3.67}$$

where J_0 is the Bessel function of the first kind of order zero and

$$u = \frac{r}{f/kw_0} \tag{3.68}$$

is a normalized transverse coordinate.

As indicated above, numerical results can readily be obtained. However, it is useful to have an analytical approximation so that OCT system parameter studies can be performed. Examination of Eq. 3.61 reveals for large values of the optical depth that Γ_{pt} is nonzero for $s\{1 - b_\phi(\rho)\}$ less than the order unity, i.e., for $b_\phi(\rho)$

near unity. Expanding $b_\phi(\rho)$ in powers of ρ and retaining the first two nonzero terms yield from Eq. 3.65 that $b_\phi(\rho) \approx (1 - \rho^2/3(\rho_\phi)^2)(1 - 2p_b)$ from which it follows that

$$\Gamma_{pt} \approx \exp\left[-2p_b s - \rho^2/\rho_0^2\right], s >> 1, \tag{3.69}$$

where the lateral coherence length, ρ_0, is defined as $\rho_0 = \rho_\phi[(3/s)/(1 - 2p_b)]^{1/2}$. It is expected that the ballistic, i.e., unscattered, component of the irradiance pattern is proportional to $e^{-\mu s z}$. Thus, by interpolation [12]

$$\Gamma_{pt} \approx \exp(-\mu_s z) + [1 - \exp(-\mu_s z)]e^{-2p_b\mu_s z}\exp\left(-\rho^2/\rho_0^2\right). \tag{3.70}$$

Substituting Eqs. 3.7 and 3.70 into Eq. 3.59 and performing the integration yield the following approximate expression for the mean irradiance distribution at the probing depth z in the tissue:

$$\langle I(\mathbf{r})\rangle \approx \frac{P_S}{\pi}\left[\frac{e^{-\mu_s z}\exp\left\{-r^2/w_H^2\right\}}{w_H^2} + \frac{(1 - e^{-\mu_s z})e^{-p_b\mu_s z}\exp\left\{-r^2/w_S^2\right\}}{w_S^2}\right]. \tag{3.71}$$

For p_b<<1 the expression can be further simplified:

$$\langle I(\mathbf{r})\rangle \approx \frac{P_S}{\pi}\left[\frac{e^{-\mu_s z}\exp\left\{-r^2/w_H^2\right\}}{w_H^2} + \frac{(1 - e^{-\mu_s z})\exp\left\{-r^2/w_S^2\right\}}{w_S^2}\right]. \tag{3.72}$$

The first term in the brackets on the right-hand side of Eq. 3.72 can be interpreted to represent the attenuated distribution obtained in the absence of the inhomogeneities, and the corresponding second term represents a broader halo resulting from scattering by the inhomogeneities. The quantities w_H and w_S are the $1/e$ irradiance radii in the absence and presence of scattering, respectively, given by

$$w_H^2 = w_0^2\left(A - \frac{B}{f}\right)^2 + \left(\frac{B}{kw_0}\right)^2, \tag{3.73}$$

$$w_S^2 = w_0^2\left(A - \frac{B}{f}\right)^2 + \left(\frac{B}{kw_0}\right)^2 + \left(\frac{2B}{k\rho_0}\right)^2. \tag{3.74}$$

For the OCT system in question,

$$w_H = \frac{f}{kw_0}, \tag{3.75}$$

$$w_S = \sqrt{w_H^2 + \left(\frac{2f}{k\rho_0}\right)^2}. \tag{3.76}$$

From Eqs. 3.58 and 3.72, an expression for the intensity is obtained:

$$\langle I_B(r)\rangle \approx \frac{p_b \mu_s dz P_s}{\pi}\left[\frac{e^{-\mu_s z}\exp\{-r^2/w_H^2\}}{w_H^2} + \frac{(1-e^{-\mu_s z})\exp\{-r^2/w_S^2\}}{w_S^2}\right]. \tag{3.77}$$

Substituting Eqs. 3.10, 3.6, 3.77, 3.54, 3.55, 3.57, and 3.70 into Eq. 3.9 and performing the indicated Gaussian integrations over $\mathbf{p}_1$,$\mathbf{p}_2$ and simplifying finally yield for p_b<<1

$$\begin{aligned}\left\langle i^2(z)\right\rangle \approx{}& \frac{8\alpha^2 P_R P_S \pi p_b \mu_s |\gamma(\tau)|^2 dz}{\pi^2 k^2} \\ &\int\left[\frac{e^{-\mu_s z}\exp\{-r^2/w_H^2\}}{w_H^2} + \frac{(1-e^{-\mu_s z})\exp\{-r^2/w_S^2\}}{w_S^2}\right]^2 d\mathbf{r}.\end{aligned} \tag{3.78}$$

Performing the integration over the probed plane in Eq. 3.12 and simplifying, the following expression for the mean square heterodyne signal current is obtained:

$$\begin{aligned}\left\langle i^2(z)\right\rangle \approx{}& \frac{4\alpha^2 P_R P_s p_b \mu_s |\gamma(2(z-l_r)/c)|^2 dz}{w_H^2 k^2} \\ &\times\left[e^{-2\mu_s z} + \frac{4e^{-\mu_s z}(1-e^{-\mu_s z})}{1+\frac{w_S^2}{w_H^2}} + (1-e^{-\mu_s z})^2\frac{w_H^2}{w_S^2}\right], \\ ={}& \left\langle i^2\right\rangle_0 \Psi(z)\end{aligned} \tag{3.79}$$

where l_r is the traversed optical path length of the reference beam and c is the speed of light in vacuum. In order to incorporate the total signal contribution obtained from within the coherence gate of the sample volume, we finally integrate (3.79) along the z-axis. This corresponds to a convolution with respect to the square modulus of the temporal coherence function $|\gamma(z/c)|^2$. Assuming a rectangular coherence function of width l_c/c, where l_c is the coherence length of the source, and $\mu_s l_c$ <<1,

$$\begin{aligned}\left\langle i^2(z)\right\rangle_{coh\_gate} &\approx \frac{\alpha^2 P_R P_s \sigma_b}{\pi w_H^2} \\ &\times \left[e^{-2\mu_s z} + \frac{4e^{-\mu_s z}(1-e^{-\mu_s z})}{1+\frac{w_S^2}{w_H^2}} + (1-e^{-\mu_s z})^2 \frac{w_H^2}{w_S^2} \right] \\ &= \left\langle i^2 \right\rangle_0 \Psi(z)\end{aligned} \tag{3.80}$$

where $\sigma_b = 4\pi p_b \mu_s l_c / k^2$ denotes the effective backscattering cross section of the backscattering volume selected by the coherence gate. The quantity $\langle i^2 \rangle_0 = \alpha^2 P_R P_S \sigma_b / \pi (w_H)^2$ is the mean square heterodyne signal current in the absence of scattering, and the term contained in the brackets is the heterodyne efficiency factor $\Psi(z)$.

References

1. D. Huang, E.A. Swanson, C.P. Lin, J.S. Schuman, W.G. Stinson, W. Chang, M.R. Hee, T. Flotte, K. Gregory, C.A. Puliafito, J.G. Fujimoto, Optical coherence tomography. Science **254**, 1178–l181 (1991)
2. J.M. Schmitt, A. Knüttel, R.F. Bonner, Measurement of optical properties of biological tissues by low-coherence reflectometry. Appl. Opt. **32**, 6032–6042 (1993)
3. J.M. Schmitt, A. Knüttel, A.S. Gandjbakhche, R.F. Bonner, Optical characterization of dense tissues using low-coherence interferometry. Proc. SPIE **1889**, 197–211 (1993)
4. J.M. Schmitt, A. Knüttel, M. Yadlowsky, M.A. Eckhaus, Optical-coherence tomography of a dense tissue: statistics of attenuation and backscattering. Phys. Med. Biol. **39**, 1705–1720 (1994)
5. M.J. Yadlowsky, J.M. Schmitt, R.F. Bonner, Multiple scattering in optical coherence microscopy. Appl. Opt. **34**, 5699–5707 (1995)
6. M.J. Yadlowsky, J.M. Schmitt, R.F. Bonner, Contrast and resolution in the optical coherence microscopy of dense biological tissue. Proc. SPIE **2387**, 193–203 (1995)
7. Y. Pan, R. Birngruber, R. Engelhardt, Contrast limits of coherence-gated imaging in scattering media. Appl. Opt. **36**, 2979–2983 (1997)
8. L.S. Dolin, A theory of optical coherence tomography. Radiophys. Quantum Electron. **41**, 850–873 (1998)
9. J.M. Schmitt, A. Knüttel, Model of optical coherence tomography of heterogeneous tissue. J. Opt. Soc. Am. A **14**, 1231–1242 (1997)
10. D.J. Smithies, T. Lindmo, Z. Chen, J.S. Nelson, T.E. Milner, Signal attenuation and localization in optical coherence tomography studied by Monte Carlo simulation. Phys. Med. Biol. **43**, 3025–3044 (1998)
11. A.F. Fercher, W. Drexler, C.K. Hitzenberger, T. Lasser, Rep. Prog. Phys. **66**, 239 (2003)
12. L. Thrane, H.T. Yura, P.E. Andersen, Analysis of optical coherence tomography systems based on the extended Huygens-Fresnel principle. J. Opt. Soc. Am. A **17**, 484–490 (2000)
13. I.V. Turchin, E.A. Sergeeva, L.S. Dolin, V.A. Kamensky, N.M. Shakhova, R. Richards-Kortum, Novel algorithm of processing optical coherence tomography images for differentiation of biological tissue pathologies. J. Biomed. Opt. **10**, 064024 (2005)
14. A. Tycho, T.M. Jørgensen, H.T. Yura, P.E. Andersen, Derivation of a Monte Carlo method for modeling heterodyne detection in optical coherence tomography systems. Appl. Opt. **41**, 6676–6691 (2002)

15. H. Kahn, T.E. Harris, Estimation of particle transmission by random sampling", in *Monte Carlo Methods*. National Bureau of Standards Applied Mathematics Series (U. S. Government Printing Office, Washington, DC, 1951)
16. B.C. Wilson, G. Adam, A Monte Carlo model for the absorption and flux distributions of light in tissue. Med. Phys. **10**, 824–830 (1983)
17. Y. Feng, R. Wang, J. Elder, Theoretical model of optical coherence tomography for system optimization and characterization. J. Opt. Soc. Am. A **20**, 1792–1803 (2003)
18. H.T. Yura, Signal-to-noise ratio of heterodyne lidar systems in the presence of atmospheric turbulence. Opt. Acta **26**, 627–644 (1979)
19. B. Karamata, M. Laubscher, M. Leutenegger, S. Bourquin, T. Lasser, P. Lambelet, Multiple scattering in optical coherence tomography. I. Investigation and modeling. J. Opt. Soc. Am. A **22**, 1369–1379 (2005)
20. J.W. Goodman, *Statistical Optics* (Wiley, New York, 1985)
21. R.G. Frehlich, M.J. Kavaya, Coherent laser radar performance for general atmospheric refractive turbulence. Appl. Opt. **30**, 5325–5352 (1991)
22. D. Arnush, Underwater light-beam propagation in the small-angle-scattering approximation. J. Opt. Soc. Am. **62**, 1109–1111 (1972)
23. H.T. Yura, A multiple scattering analysis of the propagation of radiance through the atmosphere, in *Proceedings of the Union Radio-Scientifique International Open Symposium*, (La Baule, France, 1977), pp. 65−69; see also Ref. [44], pp. 54–55
24. H.T. Yura, L. Thrane, P.E. Andersen, Closed-form solution for the Wigner phase-space distribution function for diffuse reflection and small-angle scattering in a random medium. J. Opt. Soc. Am. A **17**, 2464–2474 (2000)
25. M.G. Raymer, C. Cheng, D.M. Toloudis, M. Anderson, M. Beck, Propagation of Wigner coherence functions in multiple scattering media, in *Advances in Optical Imaging and Photon Migration*, ed. by R.R. Alfano, J.G. Fujimoto. OSA Trends in Optics and Photonics Series, vol. 2 (Optical Society of America, Washington, DC, 1996), pp. 236–238
26. C.-C. Cheng, M.G. Raymer, Long-range saturation of spatial decoherence in wave-field transport in random multiple-scattering media. Phys. Rev. Lett. **82**, 4807–4810 (1999)
27. M.G. Raymer, C.-C. Cheng, Propagation of the optical Wigner function in random multiple-scattering media, in *Laser-Tissue Interaction XI: Photochemical, Photothermal, and Photomechanical*, ed by D.D. Duncan, J.O. Hollinger, S.L. Jacques, Proc. SPIE **3914**, 376−380 (2000)
28. P. Lee, W. Gao, X. Zhang, Performance of single-scattering model versus multiple-scattering model in the determination of optical properties of biological tissue with optical coherence tomography. Appl. Opt. **49**, 3538–3544 (2010)
29. G. Yao, L.V. Wang, Monte Carlo simulation of an optical coherence tomography signal in homogeneous turbid media. Phys. Med. Biol. **44**, 2307–2320 (1999)
30. P.E. Andersen, L. Thrane, H.T. Yura, A. Tycho, T.M. Jørgensen, M.H. Frosz, Advanced modeling of optical coherence tomography systems. Phys. Med. Biol. **49**, 1307–1327 (2004)
31. L. Thrane, H.T. Yura, P.E. Andersen, Calculation of the maximum obtainable probing depth of optical coherence tomography in tissue. Proc. SPIE **3915**, 2–11 (2000)
32. I. Dror, A. Sandrov, N.S. Kopeika, Experimental investigation of the influence of the relative position of the scattering layer on image quality: the shower curtain effect. Appl. Opt. **37**, 6495–6499 (1998)
33. J.M. Schmitt, G. Kumar, Turbulent nature of refractive-index variations in biological tissue. Opt. Lett. **21**, 1310–1312 (1996)
34. J. Strohbehn (ed.), *Laser Beam Propagation in the Atmosphere* (Springer, New York, 1978)
35. R.L. Fante, Wave propagation in random media: a systems approach, in *Progress in Optics XXII*, ed. by E. Wolf (Elsevier, New York, 1985)
36. S.M. Rytov, Y.A. Kravtsov, V.I. Tatarskii, Principles of statistical radiophysics, in *Wave Propagation Through Random Media*, vol. 4 (Springer, Berlin, 1989)

37. A. Ishimaru, *Wave Propagation and Scattering in Random Media* (IEEE Press, Piscataway, 1997)
38. R.F. Lutomirski, H.T. Yura, Propagation of a finite optical beam in an inhomogeneous medium. Appl. Opt. **10**, 1652–1658 (1971)
39. Z.I. Feizulin, Y.A. Kravtsov, Expansion of a laser beam in a turbulent medium. Izv. Vyssh. Uchebn. Zaved. Radiofiz. **24**, 1351–1355 (1967)
40. J.W. Goodman, *Introduction to Fourier Optics*, 2nd edn. (McGraw-Hill, Singapore, 1996)
41. H.T. Yura, S.G. Hanson, Optical beam wave propagation through complex optical systems. J. Opt. Soc. Am. A **4**, 1931–1948 (1987)
42. H.T. Yura, S.G. Hanson, Second-order statistics for wave propagation through complex optical systems. J. Opt. Soc. Am. A **6**, 564–575 (1989)
43. A.E. Siegman, *Lasers* (University Science, Mill Valley, 1986), pp. 626–630
44. M.J.C. Van Gemert, S.L. Jacques, H.J.C.M. Sterenborg, W.M. Star, Skin optics. IEEE Trans. Biomed. Eng. **36**, 1146–1154 (1989)
45. C.F. Bohren, D.R. Huffman, *Absorption and Scattering of Light by Small Particles* (Wiley, New York, 1983)
46. D.L. Fried, Optical heterodyne detection of an atmospherically distorted signal wave front. Proc. IEEE **55**, 57–67 (1967)
47. L. Thrane, *Optical Coherence Tomography: Modeling and Applications*. PhD dissertation, Risø National Laboratory, Denmark, 2000, ISBN 87-550-2771-7)
48. L.G. Henyey, J.L. Greenstein, Diffuse radiation in the galaxy. Astrophys. J. **93**, 70–83 (1941)
49. S.L. Jacques, C.A. Alter, S.A. Prahl, Angular dependence of He-Ne laser light scattering by human dermis. Lasers Life Sci. **1**, 309–333 (1987)
50. C.M. Sonnenschein, F.A. Horrigan, Signal-to-noise relationships for coaxial systems that heterodyne backscatter from the atmosphere. Appl. Opt. **10**, 1600–1604 (1971)
51. V.V. Tuchin, S.R. Utz, I.V. Yaroslavsky, Skin optics: modeling of light transport and measuring of optical parameters, in *Medical Optical Tomography: Functional Imaging and Monitoring, IS11*, ed. by G. Mueller, B. Chance, R. Alfano et al. (SPIE Press, Bellingham, 1993), pp. 234–258
52. J.A. Izatt, M.D. Kulkarni, S. Yazdanfar, J.K. Barton, A.J. Welch, In vivo bidirectional color Doppler flow imaging of picoliter blood volumes using optical coherence tomography. Opt. Lett. **22**, 1439–1441 (1997)
53. Z. Chen, T.E. Milner, D. Dave, J.S. Nelson, Optical Doppler tomographic imaging of fluid flow velocity in highly scattering media. Opt. Lett. **22**, 64–66 (1997)
54. Y. Zhao, Z. Chen, C. Saxer, Q. Shen, S. Xiang, J.F. de Boer, J.S. Nelson, Doppler standard deviation imaging for clinical monitoring of in vivo human skin blood flow. Opt. Lett. **25**, 1358–1360 (2000)
55. H. Ren, K.M. Brecke, Z. Ding, Y. Zhao, J.S. Nelson, Z. Chen, Imaging and quantifying transverse flow velocity with the Doppler bandwidth in a phase-resolved functional optical coherence tomography. Opt. Lett. **27**, 409–411 (2002)
56. S. Yazdanfar, A.M. Rollins, J.A. Izatt, Imaging and velocimetry of the human retinal circulation with color Doppler optical coherence tomography. Opt. Lett. **25**, 1448–1450 (2000)
57. J. Kalkman, A.V. Bykov, D.J. Faber, T.G. van Leeuwen, Multiple and dependent scattering effects in Doppler optical coherence tomography. Opt. Express **18**, 3883–3892 (2010)
58. H.T. Yura, L. Thrane, P.E. Andersen, Analysis of multiple scattering effects in optical Doppler tomography. SPIE Proc. **5690**, 475–479 (2005)
59. T. Lindmo, D.J. Smithies, Z. Chen, J.S. Nelson, T.E. Milner, Accuracy and noise in optical Doppler tomography studied by Monte Carlo simulation. Phys. Med. Biol. **43**, 3045–3064 (1998)
60. A. Tycho, T.M. Jørgensen, Comment on 'excitation with a focused, pulsed optical beam in scattering media: diffraction effects. Appl. Opt. **41**, 4709–4711 (2002)
61. V.R. Daria, C. Saloma, S. Kawata, Excitation with a focused, pulsed optical beam in scattering media: diffraction effects. Appl. Opt. **39**, 5244–5255 (2000)

62. Q. Lu, X. Gan, M. Gu, Q. Luo, Monte Carlo modeling of optical coherence tomography imaging through turbid media. Appl. Opt. **43**, 1628–1637 (2004)
63. J. Schmitt, A. Knüttel, M. Yadlowski, Confocal microscopy in turbid media. J. Opt. Soc. A **11**, 2226–2235 (1994)
64. J.M. Schmitt, K. Ben-Letaief, Efficient Monte carlo simulation of confocal microscopy in biological tissue. J. Opt. Soc. Am. A **13**, 952–961 (1996)
65. C.M. Blanca, C. Saloma, Monte Carlo analysis of two-photon fluorescence imaging through a scattering medium. Appl. Opt. **37**, 8092–8102 (1998)
66. Y. Pan, R. Birngruber, J. Rosperich, R. Engelhardt, Low-coherence optical tomography in turbid tissue—theoretical analysis. Appl. Opt. **34**, 6564–6574 (1995)
67. L.-H. Wang, S.L. Jacques, L.-Q. Zheng, MCML—Monte Carlo modeling of photon transport in multi-layered tissues. Comput. Methods Prog. Biomed. **47**, 131–146 (1995)
68. S.A. Prahl, M. Keijzer, S.L. Jacques, A.J. Welch, A Monte Carlo model for light propagation in tissue", in *Dosimetry of Laser Radiation in Medicine and Biology*. SPIE Institute Series IS, vol. 5 (SPIE Press, Bellingham, 1998)
69. L. Thrane, M.H. Frosz, A. Tycho, T.M. Jørgensen, H.T. Yura, P.E. Andersen, Extraction of optical scattering parameters and attenuation compensation in optical coherence tomography images of multi-layered tissue structures. Opt. Lett. **29**, 1641–1643 (2004)
70. D.I. Hughes, F.A. Duck, Automatic attenuation compensation for ultrasonic imaging. Ultrasound Med. Biol. **23**, 651–664 (1997)
71. C. Xu, J.M. Schmitt, S.G. Carlier, R. Virmani, Characterization of atherosclerosis plaques by measuring both backscattering and attenuation coefficients in optical coherence tomography. J. Biomed. Opt. **13**, 034003 (2008)
72. A. Knüttel, S. Bonev, W. Knaak, New method for evaluation of in vivo scattering and refractive index properties obtained with optical coherence tomography. J. Biomed. Opt. **9**, 265–273 (2004)
73. G.J. Tearney, S.A. Boppart, B.E. Bouma, M.E. Brezinski, N.J. Weissman, J.F. Southern, J.G. Fujimoto, Scanning single-mode fiber optic catheter-endoscope for optical coherence tomography. Opt. Lett. **21**, 543–545 (1996)
74. L. Thrane, T.M. Jørgensen, P.E. Andersen, H.T. Yura, True-reflection OCT imaging. Proc. SPIE **4619**, 36–42 (2002)
75. R.O. Esenaliev, K.V. Larin, I.V. Larina, M. Motamedi, Noninvasive monitoring of glucose concentration with optical coherence tomography. Opt. Lett. **26**, 992–994 (2001)
76. K.V. Larin, T. Akkin, R.O. Esenaliev, M. Motamedi, T.E. Milner, Phase-sensitive optical low-coherence reflectometry for the detection of analyte concentrations. Appl. Opt. **43**, 3408–3414 (2004)
77. V.M. Kodach, D.J. Faber, J. van Marle, T.G. van Leeuwen, J. Kalkman, Determination of the scattering anisotropy with optical coherence tomography. Opt. Express **19**, 6131–6140 (2011)
78. D.J. Faber, M.C.G. Aalders, E.G. Mik, B.A. Hooper, M.J.C. van Gemert, T.G. van Leeuwen, Oxygen saturation-dependent absorption and scattering of blood. Phys. Rev. Lett. **93**(028102), 1–4 (2004)
79. D.J. Faber, E.G. Mik, M.C.G. Aalders, T.G. van Leeuwen, Toward assessment of blood oxygen saturation by spectroscopic optical coherence tomography. Opt. Lett. **30**, 1015–1017 (2005)
80. F.J. van der Meer, D.J. Faber, D.M.B. Sassoon, M.C. Aalders, G. Pasterkamp, T.G. van Leeuwen, Localized measurement of optical attenuation coefficients of atherosclerotic plaque constituents by quantitative optical coherence tomography. IEEE Trans. Med. Imaging **24**, 1369–1376 (2005)
81. G. van Soest, T. Goderie, E. Regar, S. Koljenovic, G.L.J.H. van Leenders, N. Gonzalo, S. van Noorden, T. Okamura, B.E. Bouma, G.J. Tearney, J.W. Oosterhuis, P.W. Serruys, A.F.W. van der Steen, Atherosclerotic tissue characterization in vivo by optical coherence tomography attenuation imaging. J. Biomed. Opt. **15**, 011105 (2010)

82. T. Kubo, C. Xu, Z. Wang, N.S. van Ditzhuijzen, H.G. Bezerra, Plaque and thrombus evaluation by optical coherence tomography. Int. J. Cardiovasc. Imaging **27**, 289–298 (2011). doi:10.1007/s10554-010-9790-1
83. Q.Q. Zhang, X.J. Wu, T. Tang, S.W. Zhu, Q. Yao, B.Z. Gao, X.C. Yuan, Quantitative analysis of rectal cancer by spectral domain optical coherence tomography. Phys. Med. Biol. **57**, 5235–5244 (2012). doi:10.1088/0031-9155/57/16/5235
84. O.K. Adegun, P.H. Tomlins, E. Hagi-Pavli, G. Mckenzie, K. Piper, D.L. Bader, F. Fortune, Quantitative analysis of optical coherence tomography and histopathology images of normal and dysplastic oral mucosal tissues. Lasers Med. Sci. **27**, 795–804 (2012). doi:10.1007/s10103-011-0975-1
85. P.D. Woolliams, P.H. Tomlins, The modulation transfer function of an optical coherence tomography imaging system in turbid media. Phys. Med. Biol. **56**, 2855–2871 (2011). doi:10.1088/0031-9155/56/9/014
86. N.M. Shakhova, V.M. Gelikonov, V.A. Kamensky, R.V. Kuranov, I.V. Turchin, Clinical aspects of the endoscopic optical coherence tomography: a method for improving the diagnostic efficiency. Laser Phys. **12**, 617–626 (2002)
87. D. Levitz, L. Thrane, M.H. Frosz, P.E. Andersen, C.B. Andersen, J. Valanciunaite, J. Swartling, S. Andersson-Engels, P.R. Hansen, Determination of optical scattering properties of highly-scattering media in optical coherence tomography images. Opt. Express **12**, 249–259 (2004)
88. W.-C. Kuo, M.-W. Hsiung, J.-J. Shyu, N.-K. Chou, P.-N. Yang, Assessment of arterial characteristics in human atherosclerosis by extracting optical properties from polarization-sensitive optical coherence tomography. Opt. Express **16**, 8117–8125 (2008)
89. H.T. Yura, S.G. Hanson, Effects of receiver optics contamination on the performance of laser velocimeter systems. J. Opt. Soc. Am. A **13**, 1891–1902 (1996)
90. V.I. Tatarskii, *The Effects of the Turbulent Atmosphere on Wave Propagation* (National Technical Information Service, Springfield, 1971)
91. A.N. Yaroslavsky, I.V. Yaroslavsky, T. Goldbach, H.-J. Schwarzmaier, Influence of the scattering phase function approximation on the optical properties of blood determined from the integrating sphere measurements. J. Biomed. Opt. **4**, 47–53 (1999)
92. M. Stone, Cross-validatory choice and assessment of statistical predictions. J. R. Stat. Soc. B **36**, 111–147 (1974)